Revision 2

Using pyrite composition to track the multi-stage fluids superimposed on a porphyry Cu system

Chao Wu[a, b, c, d], David R. Cooke[c, d], Michael J. Baker[c, d], Lejun Zhang[c, d], Pei Liang[f], Jing Fang[a], Paul Olin[d], Leonid V. Danyushevsky[g], Huayong Chen[a, b, e, †]

[a]*Key Laboratory of Mineralogy and Metallogeny, Guangzhou Institute of Geochemistry, Chinese Academy of Sciences, Guangzhou 510640, China*

[b]*CAS Center for Excellence in Deep Earth Science, Guangzhou, 510640, China*

[c]*ARC Research Hub for Transforming the Mining Value Chain, TMVC, University of Tasmania, Private Bag 79, Hobart, Tasmania 7001, Australia*

[d]*CODES, Centre for Ore Deposit and Earth Sciences, University of Tasmania, Hobart, Australia*

[e]*University of Chinese Academy of Sciences, Beijing 100049, China*

[f]*Civil and Resource Engineering School, University of Science & Technology Beijing, Beijing, 100083*

[g]*Hobart, Tasmania, Australia*

[†]Corresponding Author: *Huayong Chen*, e-mail: *huayongchen@gig.ac.cn*

Abstract

The Yulekenhalasu porphyry Cu–Mo deposit (0.2 Mt Cu at 1.04 wt. % and 0.012 Mt Mo at 0.06 wt. %) is located in the Devonian Halasu copper belt, East Junggar block, northwest China. At Yulekenhalasu, Cu and Mo mineralization commonly occurs as disseminated sulfides or veinlets in porphyry-related alteration zones. Five alteration stages have been identified, including porphyry-type alteration, i.e., sodic-calcic (stage I), potassic (stage IIa), propylitic (stage IIb), and phyllic (stage III) alteration, and widespread late Cu sulfide-bearing veins (stage IV) crosscutting porphyry-type alteration, plus a post-ore fault-

controlled argillic alteration (stage V). Stages IV and V have overprinted porphyry-type alteration (stages I–III).

Anomalous concentrations of trace elements in stage IIb pyrite (e.g., Ti, Zr, Gd, and Hf) are due to the presence of micro-inclusions (e.g., zircon and rutile) in the low-temperature (~200 °C) propylitic zone. Copper, Ag, Co, and Mn, occurring as stoichiometric substitutions or as tetrahedrite inclusions in overprinting stage IV pyrite, were sourced directly from the primary hydrothermal fluid. The enrichment of distal pathfinder elements (e.g., Cr, Au, and Tl) in overprinting stage V pyrite was caused by a low-temperature (~160 °C) hydrothermal event related to regional orogenic Au mineralization. The spatial variation of Se/S in pyrite among various paragenetic stages were influenced by changes in the hydrothermal fluid composition and temperature, with the latter having the effect of decreasing pyrite Se/S. Lower Se concentrations in pyrite of stages IIb and III close to the orebody are explained by relatively higher temperatures in the locus of mineralization. This may provide a potential vectoring tool to mineralization using pyrite geochemistry in porphyry deposits.

Systematic thermodynamic calibrations were applied to pyrite compositions to fingerprint the corresponding Se/S and Co/Ni ratios of fluids and further to develop a complete metallogenic model for Yulekenhalasu. The Devonian diorite porphyry generated fluids that produced the early porphyry-type alteration. High Co/Fe (average ~1 x 10^{-4}) and Ni/Fe (average ~3 x 10^{-6}) ratios of fluid for late Cu sulfide-bearing veins, combined with higher Se/S (average ~6 x 10^{-7}) than orogenic Au deposits (average ~3 x 10^{-8}), indicate the fluids possibly derived from a Late Devonian-Carboniferous mafic intrusion. Argillic alteration assemblages forming at ca. 280 Ma host pyrite relatively enriched in Au (average 0.1 ppm, with native gold inclusions). Therefore it is likely related to a regional orogenic gold mineralizing event in the Early Permian that overprinted Devonian mineralization. Although spatially contiguous, hydrothermal alteration and hypogene mineralizing stages identified herein represent discrete episodes of hydrothermal activities at Yulekenhalasu. The multi-stage alteration features observed at Yulekenhalasu may provide insights into the complete evolutionary history of Paleozoic porphyry Cu deposit systems in the Central Asian orogenic

belt. This study contributes to a better understanding of the metallogenic and exploration models of porphyry Cu deposits overprinted by multi-stage hydrothermal events, which is economically important in Phanerozoic orogenic belts.

Keywords: Central Asian Orogenic Belt, Yulekenhalasu, porphyry Cu-Mo deposit, pyrite composition, superimposed alteration and mineralization

Introduction

The Central Asian Orogenic Belt is one of the world's largest subduction-accretionary orogens (Carroll et al., 1990; Jahn, 2004; Jahn et al., 2000; Mossakovsky et al., 1994; Sengör et al., 1993; Xiao et al., 2009b; Fig. 1a). It hosts several giant porphyry Cu deposits including Oyu Tolgoi, Erdenet, and Aktogai-Aiderly, and is one of the most important porphyry Cu belts in the world in terms of proven resources (Mao et al., 2014; Perelló et al., 2001; Seltmann et al., 2014; Yakubchuk, 2004; Yakubchuk et al., 2012). Most of the porphyry deposits in the Central Asian Orogenic Belt formed in island- or continental-arc settings, but were subject to Late Paleozoic collision and subsequent post-collisional and intra-plate extension, e.g., Tuwu-Yandong (Wang et al., 2019; Xiao et al., 2017), Yuhai (Wang et al., 2018), and Sanchakou Cu deposits (Qin et al., 2009; Wang et al., 2022), creating challenges and opportunities for mineral exploration (Heinhorst et al., 2000; Nie et al., 2004; Yakubchuk, 2004; Zhao et al., 1997). The Yulekenhalasu deposit, with a metal tonnage greater than 0.2 Mt Cu and an average grade at 1.04 % Cu (Xiang, 2013) is one of the earliest discovered porphyry Cu deposits in the Chinese Altay – East Junggar orogenic belt (Fig. 1). Previous studies of the deposit have focused on magmatism (Wu et al., 2015; Yang et al., 2014), quartz-hosted fluid inclusions (Geng et al., 2013; Yang et al., 2012), and trace element variations in sulfides (Hong et al., 2021b; Hong et al., 2018). These studies suggest that the Devonian Yulekenhalasu system is characterized by typical porphyry-type mineralization and alteration but was overprinted by late-stage hydrothermal events (Hong et al., 2021b; Liu et al., 1991; Wu et al., 2015; Xue et al., 2016; Yan et al., 2006; Yang et al., 2014). However, previous studies lumped multiple alteration stages into porphyry-type and overprinting

categories, which lack detailed descriptions, and models for their origins and conditions of formation during multi-stage hydrothermal events in different tectonic settings are poorly understood.

To describe the detailed paragenetic history of Yulekenhalasu, we present new geological observations and geochemical data obtained from LA–ICP–MS analyses of hydrothermal pyrite sampled from a selection of alteration zones across the deposit. These new data are used to constrain the complex hydrothermal evolution of Yulekenhalasu. Furthermore, a new metallogenic model for porphyry deposits that preserve the overprint of multi-stage hydrothermal events, which are ubiquitous in the Central Asian Orogenic Belt, is developed to guide the exploration of porphyry Cu deposits in orogenic belts with prolong evolutionary histories.

Regional geological setting

The Yulekenhalasu porphyry Cu deposit is located on the northern margin of the East Junggar belt. It is part of the Halasu copper belt, which contains, from north to south, the Yulekenhalasu, Dunke'erman, and Halasu I, II and III copper deposits (Fig. 1). Halasu I (0.17 Mt Cu with an average grade of 0.34 % Cu) and Yulekenhalasu are the two largest deposits in the belt (Xiang, 2013; Yang et al., 2014).

Four distinct metallogenic belts were recognized in the Chinese Altay – East Junggar region by Wan et al. (2017) and Yang et al. (2018a), including a volcanogenic massive sulfide (VMS) Cu–Pb–Zn belt and a rare metal pegmatite belt in the Chinese Altay, a shear zone-hosted Au (or orogenic Au) belt along the Erqis fault, and a porphyry Cu–Mo ± Au belt in East Junggar (Fig. 1c). The VMS deposits (e.g., Ashele Cu–Zn deposit) formed in the Lower to Middle Devonian extensional arc-related submarine basins, and shear zone-hosted Au deposits (e.g., Kekesayi and Kubusu Au deposits) formed at the Early Permian transpressional terrane boundaries (Niu et al., 2020; Wan et al., 2014; Yang et al., 2018a; Yang et al., 2018b). The East Junggar porphyry deposits formed in three periods at convergent continental margins: ca. 408 Ma (e.g., Hersai; Du et al., 2010), 375 Ma (e.g.,

Halasu; Yang et al., 2014) and 330 Ma (e.g., Xilekuduke; Long et al., 2011; Wan et al., 2014). East Junggar also hosts the Qiaoxiahala (383.2 ± 4.5 Ma) and Laoshankou (375.2 ± 2.6 Ma) IOCG deposits (Li et al., 2014), and the Kalatongke Cu–Ni magmatic sulfide deposit (287 ± 5 Ma; Han et al., 2004; Fig. 1c).

The Chinese Altay in the northern Chinese Altay–East Junggar zone comprises Middle Ordovician to Late Carboniferous metamorphosed clastic turbidite, limestone, sandstone-shale and island arc-related pyroclastic rocks (Xiao et al., 2009b; Yang et al., 2014; Fig. 1; Zhang et al., 2009). The Erqis shear zone separates the Chinese Altay from East Junggar (Fig. 1), and contains high-grade gneiss and schist, Paleozoic ophiolitic fragments and mafic-intermediate lavas (Xue et al., 2016; Fig. 1c; Yang et al., 2014). Intrusions exposed in the Chinese Altay and Erqis shear zone are divided into two subgroups: Upper Ordovician to Devonian calc-alkaline granitoids (ca. 450 – 375 Ma) and Carboniferous to Early Permian alkaline granitoids (ca. 340 – 280 Ma; Wang et al., 2010). The East Junggar terrane contains minor Silurian sedimentary rocks, extensive exposures of Devonian mafic-intermediate volcanic rocks and marine sedimentary rocks, Early to Middle Carboniferous intermediate volcanic- and sedimentary rocks, and Early Permian continental volcanic rocks (Xiao et al., 2009a). In addition to the Devonian to Early Carboniferous calc-alkaline granites and adakites that formed in an island arc setting, East Junggar also contains minor Late Carboniferous and Permian A-type granite dykes, interpreted to have been emplaced in a post-orogenic environment (Wang et al., 2010; Fig. 1c; Xiao et al., 2009a).

The Erqis shear zone and the Abagong fault are terrane-boundary fault systems within the Chinese Altay–East Junggar (Fig. 1b). Fault systems in East Junggar are mainly NW-trending thrusts (e.g., Armantai and Kelameili faults) and NNW-trending strike-slip faults (e.g., Fuyun fault; Windley et al., 2002; Fig. 1b, c). The Fuyun fault (also referred to as the Keketuohai–Ertai fault) is a 180-km-long active oblique strike-slip fault that marks the western margin of the Halasu copper belt. It dextrally displaced the Erqis fault by 7 to 8 km (Windley et al., 2002; Fig. 1c), with the Yulekenhalasu deposit sandwiched by the Erqis shear zone to the northwest and Fuyun fault to the west.

Deposit geology

Exposed in the area surrounding Yulekenhalasu is a succession of marine volcanic and volcaniclastic rocks consisting principally of the Middle Devonian Beitashan Formation, a sequence of mafic to intermediate lava and tuffs, breccia and sandstone (Hong et al., 2021a; Hong et al., 2017). The Beitashan Formation is unconformably overlain by the Early Carboniferous Jiangbasitao Formation, which consists of, from bottom to top, carbonaceous black shale, siltstone (partially metamorphosed into slate), conglomerate, tuffaceous sandstone, and intermediate tuff intercalated with minor andesite that was deposited in a volcanic arc setting (Zhang et al., 2009). Of the three principal fault orientations recognized in the district (NNW-, NE- and W-trending fault systems; Figs. 1c and 2), the NNW-trending fault system is parallel to the elongated axis of the principal orebodies at Yulekenhalasu and appears closely associated with the regional Fuyun fault which dips steeply to the northeast. West-trending faults are inferred to record sinistral strike-slip movement, whereas the NE-trending faults are tensional faults with sinistral movement (Liu et al., 2010).

Intrusive rocks of Middle Devonian to Carboniferous age include a pre-mineralization porphyritic syenite (ca. 390 Ma), syn-mineralization quartz diorite and diorite porphyry (ca. 382–372 Ma), and post-mineralization quartz granite porphyry and alkali granite porphyry (ca. 350–320 Ma; Wu et al., 2015; Xiang et al., 2012; Yang et al., 2014). The emplacement of granitoids was generally controlled by the NW-trending fault system, and the intrusions have been cross-cut by W-trending faults (Fig. 2b). The porphyritic syenite occurs as NW-trending stocks and contains coarse-grained K-feldspar as phenocrysts within a groundmass of fine-grained quartz and K-feldspar. The Jiangbasitao Formation is separated from an underlying diorite porphyry by a NW-trending fault (Fig. 2b). The quartz diorite crops out as a large stock along the southern margin of the district, where it intruded the Beitashan Formation (Fig. 2b). It contains plagioclase, quartz, and biotite, with minor alkali feldspar, titanite, apatite, magnetite, and zircon. The diorite porphyry contains phenocrysts of plagioclase, quartz, K-feldspar, minor biotite and hornblende in a groundmass of plagioclase, quartz and

biotite. Post-mineralization quartz granite porphyry dykes that cut the Jiangbasitao Formation are characterized by quartz and minor plagioclase phenocrysts in a groundmass of quartz, plagioclase and biotite (Yang et al., 2014). The alkali granite porphyry is dominated by coarse-grained K-feldspar and minor biotite phenocrysts within a groundmass of fine-grained K-feldspar, quartz and biotite (Wu et al., 2015).

Two mineralized zones (west and east) have been recognized at Yulekenhalasu (Fig. 2b). The eastern zone occurs within the diorite porphyry and is host to the main copper reserve; it is ~800 m long and 20 m to 120 m wide (Fig. 2b). The western zone is hosted by basalt and porphyritic syenite in the NW part of the district and is 300 m long and 10–80 m wide. It has been subdivided into three smaller mineralized bodies. Sulfides at Yulekenhalasu include chalcopyrite, pyrite and molybdenite, with lesser amounts of bornite, galena, sphalerite, and pyrrhotite (Fig. 3). Gangue minerals are dominated by quartz, K-feldspar, magnetite, biotite, gypsum, sericite, chlorite, epidote and calcite (Fig. 3). Ore minerals occur in various textural forms including disseminated grains, veinlets, stockwork veins, replacements, and as cataclasites in fault zones.

Paragenesis

Five hydrothermal alteration and hypogene mineralizing stages have been identified with stage II consist of two identifiable alteration assemblages (i.e., IIa and IIb), along with a supergene process at Yulekenhalasu, based on field relationships, including overprinting, crosscutting, and alteration mineral assemblages (Fig. 3). Their spatial distributions are displayed in Figure 2.

Stage I: Sodic-calcic alteration

This stage comprises abundant magnetite, actinolite, plagioclase, minor epidote and biotite, and traces of quartz (Fig. 3). Arancibia and Clark (1996) and Sillitoe (2010) interpreted this type of magnetite-actinolite-plagioclase-dominated alteration as one of the earliest-forming alteration assemblages, implying an oxidized, sulfur-deficient initial fluid.

The alteration assemblage is characterized by randomly oriented subhedral to euhedral magnetite grains that replaced primary mafic minerals (e.g., amphibole and biotite) in both the phenocrysts and groundmass of the diorite porphyry (Fig. 4a). The presence of actinolite along with plagioclase (± albite) and minor epidote implies addition of Ca and Na to the host rock. Where both magnetite and plagioclase are abundant in the diorite porphyry, the preservation of primary textures is rare (Fig. 4a). Pyrite occurs as disseminated grains with magnetite and chlorite-altered actinolite. Subhedral pyrite grains contain rare chalcopyrite inclusions and disseminated magnetite along their rims. The sodic-calcic alteration zone at Yulekenhalasu ranges from 10 to 50 m thick and is preserved in the diorite porphyry adjacent to andesitic and basaltic wall rocks (Fig. 2a). It occurs adjacent to the orebody and is poorly mineralized relative to later alteration assemblages.

Stage IIa: Potassic alteration

The potassic alteration zone comprises abundant K-feldspar and quartz, together with lesser biotite, anhydrite and magnetite, and traces of apatite and titanite (Fig. 3). The reddish potassic-altered diorite porphyry contains fine-grained secondary K-feldspar, quartz and minor magnetite, which have partially to completely destroyed primary mineral textures (Fig. 4b). K-feldspar and quartz selectively replaced primary feldspars in the groundmass, whereas primary mafic minerals (e.g., amphibole and biotite) were replaced by fine-grained biotite that was subsequently altered locally to muscovite or chlorite. Quartz veins that contain molybdenite and biotite are common in the potassic zone. They have been cut by late calcite veinlets (Fig. 4c). Hypogene Cu mineralization is mainly associated with K-feldspar-dominated potassic alteration, with abundant chalcopyrite occurring as disseminations or veinlets in the host diorite. Euhedral pyrite crystals in this assemblage are commonly surrounded by chalcopyrite (Fig. 4d). Spatially, the majority of hypogene mineralization at Yulekenhalasu is hosted within the potassic-altered diorite porphyry and is adjacent to the underlying porphyritic syenite (Fig. 2a), with the potassic alteration zone accounting for approximately 90 % of Cu metal reserves.

Stage IIb: Propylitic alteration

The propylitic alteration zone, forming a halo around the potassic zone, is inferred to have formed at the same time from the spent fluids from the potassic alteration migrating away from the porphyry center. The zone is characterized by veinlets or aggregate patches of chlorite + pyrite, planar epidote + chlorite, and locally by thick veins (~1 cm) of quartz + gypsum + chlorite in the diorite porphyry and surrounding volcanic wall rocks (Figs. 3, 4e). Propylitic-altered rocks peripheral to the deposit are commonly dark green and contain alteration assemblages dominated by chlorite, epidote, calcite, quartz, and minor actinolite and gypsum (Fig. 3).

Fine-grained epidote occurs with chlorite, calcite and minor actinolite and has replaced primary amphibole and plagioclase (Fig. 4e). Chlorite commonly occurs as aggregates or veinlets in the groundmass of the diorite porphyry, or pseudomorphs of primary amphibole and biotite crystals. Propylitic alteration is developed along the margin of the sodic-calcic alteration zone and extends through the diorite porphyry to the surrounding andesitic and basaltic wall rocks (Fig. 2a). The propylitic assemblage contains rare, disseminated pyrite grains and no chalcopyrite.

Stage III: Phyllic alteration

The phyllic alteration zone at Yulekenhalasu consists mainly of quartz, pyrite, muscovite and chlorite, as well as minor illite (Figs. 3, 4f–h). Rocks that have undergone phyllic alteration are gray and show partial to complete replacement of primary plagioclase and mafic minerals (e.g., amphibole and biotite) by secondary muscovite and chlorite, respectively (Fig. 4f, g). Chlorite occurs locally as wormy veinlets concomitant with pyrite patches (Fig. 4f). The phyllic assemblage is commonly associated with quartz veins up to several centimeters wide that have pervasive halos of muscovite and/or illite. The superposition of phyllic alteration on earlier formed potassic alteration assemblages resulted in the alteration of secondary biotite to chlorite and muscovite (Fig. 4h) and of

magnetite to hematite. Pyrite is the dominant sulfide in phyllic-altered rocks and occurs extensively as medium- to fine-grained anhedral nodules. Minor chalcopyrite is present as small inclusions in pyrite. Phyllic alteration at Yulekenhalasu has superimposed on early-formed alteration assemblages, typically at shallower levels relative to deep-seated sodic-calcic and potassic zones (Fig. 2a).

Stage IV: Late Cu sulfide-bearing veins

Widespread late-stage Cu-bearing hydrothermal veins at Yulekenhalasu overprinted earlier alteration assemblages and contributed substantially to the overall Cu resource. They vary from irregular, discontinuous, and segmented, to regular, continuous and parallel veins up to several centimeters wide (Fig. 5a, b). They mainly occur in the core of the deposit, but in some cases occur on the periphery of the potassic zone. The veins are characterized by several assemblages: pyrite + chalcopyrite + anhydrite (Vein a), pyrite + chalcopyrite + sphalerite (Vein b), bornite + pyrite + chalcopyrite (Vein c), and quartz + epidote + K-feldspar + bornite + pyrite + chalcopyrite (Vein d; Fig. 3). All vein types have sharp contacts with the potassic- and phyllic-altered diorite porphyry (Fig. 5a). The lack of associated alteration halos indicates that these Cu sulfide-bearing veins are distinct from Stage III phyllic veins and may have formed by late-stage open-space filling, rather than synchronous with potassic alteration. Euhedral quartz, locally present in some veins, shows undulose extinction and hosts abundant fluid inclusions. Pyrite generally occurs as euhedral crystals without inclusions. Minor sphalerite occurs on the margin of pyrite grains and as isolated crystals in coexisting chalcopyrite (Fig. 5b). The late Cu sulfide-bearing veins are locally responsible for hypogene upgrading and account for roughly 5 % of the Cu metal reserves.

Stage V: Argillic alteration

The argillic alteration zone at Yulekenhalasu is characterized by fine-grained quartz, kaolinite, muscovite and illite, which have completely replaced precursor minerals and destroyed primary textures (Figs. 3, 5c–e). Although there is similarity in mineral

assemblages between the phyllic and argillic alteration zones, the transition from phyllic-dominated to argillic-dominated alteration assemblages is characterized by decreasing abundance of chlorite and pyrite and increasing abundance of illite and kaolinite. The argillic alteration zone contains planar pyrite ± galena ± anhydrite ± calcite veins up to several centimeters wide (Fig. 5c–e). These veins locally developed as fissures crosscutting potassic alteration assemblages and are orientated along the tensile fractures caused by dextral shearing (Fig. 5d). Pyrite in these veins occurs as subhedral to euhedral crystals with occasional magnetite inclusions (Fig. 5e). Although the similarities in mineral assemblages between the phyllic and argillic alteration zones make it difficult to define the boundary between them at depth, argillic alteration near-surface is generally restricted to shear zones parallel to the NNW-trending fault system in the eastern mineralized zone (Fig. 2b, c) and to the NW-trending fault system in the western zone (Fig. 2b), where it is separated from the phyllic alteration zone by a sharp faulted contact (Fig. 2d).

Supergene alteration

Most mineralized rocks at Yulekenhalasu exposed at the surface or at shallow depths have been subject to supergene oxidation processes (Yang et al., 2014), with hematite, malachite and minor jarosite and covellite commonly replacing primary sulfides (Fig. 3). Supergene enrichment at Yulekenhalasu extends tens of meters deep locally and is particularly intense in strongly faulted areas with substantial malachite mineralization at fault contacts (Fig. 5f).

Pyrite composition

Sampling

To help constrain the chemical evolution of the hydrothermal fluids and assist in paragenetic interpretation, representative pyrite grains were analyzed from several alteration and mineralized zones at Yulekenhalasu. The samples analyzed include four from

the sodic-calcic alteration zone (Py_I; Fig. 4a), six from the potassic zone (Py_{IIa}; Fig. 4b, c), five from the propylitic zone (Py_{IIb}), twelve from the phyllic alteration zone (Py_{III}; Fig. 4f, g), four from late Cu sulfide-bearing veins (Py_{IV}; Fig. 5a), and two from the argillic alteration zone (Py_V; Fig. 5c, d). To compare magmatic-hydrothermal pyrite composition with pyrite of sedimentary origin, three examples of pyrite characterized by microcrystalline pyrite aligned parallel to bedding texture in the overlying sedimentary rocks of the Jiangbasitao Formation were also analyzed (Py_S).

LA–ICP–MS analysis method

All selected pyrite grains were analyzed at the LA–ICP–MS facility at CODES, University of Tasmania, using a RESOlution laser platform, equipped with a Coherent COMPex Pro 193 nm excimer laser and Lauren Technic S155 large format sample cell, coupled to an Agilent 7700 or 7900 quadrupole ICP-MS. Laser spot size is 29 μm for all pyrite and 51 μm for STDGL3 standard glass. A combination of spot analysis and elemental mapping generated by rastering a focused laser beam across the mineral surface were attempted. To calculate concentrations, the average of the signal over the time interval of interest is calibrated against reference standard STDGL3, an in-house standard sulfide-rich glass for primary calibration for quantifying siderophile and chalcophile elements (Danyushevsky et al., 2011). Data reduction and processing of the laser images was performed using CODES in-house routines. The error on average that is estimated from the standards is <5 %, which was insignificant in comparison to the samples because the majority of analyzed elements in pyrite showed several orders of magnitude variation in concentration. Full analytical details are provided in ESM 1.

Results

Representative pyrite major and trace element concentrations (S, Co, Se, Ni, As, Ti, Cr, Cu, Mn, Zn, Te, Pb, Mg, Sb, Bi, Sn, Ag, V, Cd, Mo, Tl, Gd, Au, Zr, Hf, W, Nb, Th, U and Ta) are listed in ESM 2 and illustrated in part in Figure 6. It should be noted that approximately 2,000

inclusion-free data points for argillic Py_V acquired from elemental mapping following the studies of Acosta-Góngora et al. (2022) and Sykora et al. (2018) are added to the dataset for comparison.

Paragenetic variations of pyrite composition

Comparison of trace element variability in pyrite across all hydrothermal alteration stages at Yulekenhalasu indicates that Py_{IV} and Py_V have relatively high concentrations of pathfinder trace elements, e.g., Co, Ni, As, Sb, Se, Cu, Ag, Tl, Au, Te, Mo, and W (Fig. 6), which may provide vectoring information to the locus of porphyry mineralization (Cooke et al., 2014; Sykora et al., 2018). Moreover, Py_S hosted in sedimentary rocks show remarkable enrichment in Th, Mo and W relative to hydrothermal pyrites at Yulekenhalasu. They are interpreted to be of sedimentary origin based on their microcrystalline texture aligned parallel to bedding and Co/Ni values below 2 (c.f. Large et al., 2014). Trace element concentrations in the various paragenetic stages of pyrite show some distinctive traits with enrichment of As in sodic-calcic alteration, Ti, Zr, Gd, Hf, Th, U, and Nb in propylitic alteration, Co, Mn, Cu, Ag, Zn, Sn, and V in late Cu sulfide-bearing veins, and Cr, Tl, Au, Mo, W, and Sb in argillic alteration, respectively (Fig. 6; ESM 2). Nickel is depleted in pyrite from sodic-calcic alteration, Te is characteristically depleted in sodic-calcic and potassic pyrite, Pb and Bi are depleted in potassic and propylitic pyrite, and Se is depleted in propylitic pyrite relative to the measured abundances in other alteration stages (Fig. 6). In general, Py_{III} has trace element compositions that range between early porphyry and late vein stages, without notable enrichment or depletion compared to other pyrite types.

Spatial variation in pyrite composition

Representative trace element abundances in pyrite for each hydrothermal stage have been plotted spatially on longitudinal sections in Figure 7 (Cu, Co, and Ni) and ESM 3 (As, Se, and Au). It should be noted that no spatial trends could be identified for elements in stage V (argillic alteration), due to the limited data available for these longitudinal sections. To

351 evaluate the enrichment or depletion of elements around the deposit center, we developed a
352 quantitative method to evaluate the distances of sampling locations to the orebody.
353 Specifically, the spatial extent of the orebody is simplified as an ellipse in sections, and the
354 sum of distances of certain sampling locations to two focus points of the defined ellipse
355 serves as the quantitative measurement of proximity to the orebody. Consequently, high
356 distance values are distal to the deposit center and low distance values are proximal, as
357 illustrated in the schematic diagram (Fig. 8a). Spatial trends of analyzed elements in
358 different paragenetic stages, which are highlighted by dotted arrows, are revealed by the
359 average and median values of analyses from the same sample (Fig. 8b-f; ESM 4).

360 Among pyrite of stages I–IV, Cu is the main element whose concentration appears
361 associated with mineralization. It has high concentrations (>10 ppm) in pyrite near the
362 deposit center in paragenetic stages IIa (Figs. 7c, 8b), IIb (Figs. 7d, 8c), and III (Figs. 7e, 8d).
363 Cobalt also has high concentrations in pyrite close to the deposit center, particularly in
364 stages IIa (Figs. 7i, 8e), and IIb (Figs. 7j, 8f), but not in stages I (Fig. 7h; ESM 4a), III (Fig. 7k;
365 ESM 4b) or IV (Fig. 7l; ESM 4c). Nickel has a similar spatial enrichment pattern to Co in stage
366 IIb (Figs. 7j, 7p, and 8f; ESM 4d), but differs for stage IV (Fig. 7r; ESM 4e), where the highest
367 Ni concentrations occur at shallow levels relative to Co (Fig. 7l; ESM 4c).

368 Arsenic is distinctly enriched in pyrite at deeper levels in stages IIa (ESM 3c and 4f) and
369 IV pyrites (ESM 3f and 4g). Selenium is enriched in the peripheral zone (>800 m away from
370 center) surrounding the deposit center in stages IIb (ESM 3j and 4h) and III (ESM 3k and 4i),
371 whereas high Se concentrations occur proximal to the ore body in stages I (ESM 3h and 4j)
372 and IIa (ESM 3i and 4k). Similar trends were also noted for Au (ESM 3m-r, 4l, and 4m),
373 except in stage IIb (ESM 3p and 4n), where high Au concentrations are present proximal to
374 the deposit center.

375 *Determination of fluid compositions by pyrite geochemistry and temperatures*

376 Selenium is one of the most abundant elements occurring as a stoichiometric
377 substitution for sulfur in pyrite (Diener et al., 2012; Keith et al., 2018; Layton-Matthews et

al., 2008). Although the aqueous geochemistry of Se was discussed by D'yachkova and Khodakovsky (1968) and Yamamoto (1976), the influence of temperature and hydrothermal fluid compositions on Se incorporation into pyrite remains unclear. Temperature has been interpreted to have either a positive effect on Se concentrations in pyrite (i.e., high temperature favors high Se concentration in pyrite; Layton-Matthews et al., 2008; Tischendorf, 1966; Wohlgemuth-Ueberwasser et al., 2015) or a negative effect (i.e., high temperature favors low Se concentration in pyrite; Hawley and Nichol, 1959; Huston et al., 1995; Lorand et al., 2003). To determine the behavior of Se in pyrite, we conducted modeling based on Reaction A as described by Huston et al. (1995), with modeled ratios of H_2Se/H_2S in fluid illustrated in Figure 9. The full detailed process of Se/S modeling and scalar calculations is provided in ESM 1. The balanced equation for Reaction A from Huston et al. (1995) is:

$$FeS_2\ (s) + 2H_2Se\ (aq) \leftrightarrow FeSe_2\ (s) + 2H_2S\ (aq) \quad (A)$$

As shown in Figure 9a, the molar ratios of Se/S in pyrite generally decrease with increasing temperature under a constant ratio of Se/S in the fluid when equilibrium balance is reached. Moreover, at temperatures below 300 °C, Se/S in pyrite is dominated by both temperature and Se/S in hydrothermal fluid, but the influence of temperature becomes negligible above 300 °C (Fig. 9a) which may explain the geological observations of the non-uniform temperature dependence of Se in pyrite. Because Se concentrations in pyrite can record the Se of parental hydrothermal fluid (Huston et al., 1995), combining our measured Se concentrations in pyrite with the fluid inclusion results of Wu (2018) can provide rough estimates of Se/S ($\sim 3 \times 10^{-8} - 1 \times 10^{-6}$) in the hydrothermal fluids (Fig. 9a).

The ratio of Co/Ni in pyrite has long been used as an indicator for ore genesis (Bajwah et al., 1987; Bralia et al., 1979; Loftus-Hills and Solomon, 1967). Due to the apparent dependence of Co/Ni on various factors, e.g., temperature, fluid composition, and ore-forming processes (Bajwah et al., 1987; Bralia et al., 1979; Campbell and Ethier, 1984; Loftus-Hills and Solomon, 1967), the use of Co/Ni requires supporting evidence to help interpret magmatic-hydrothermal processes in the ore-forming environment.

Based on a similar hypothesis to Se substitution in pyrite, we proposed a novel approach to link Co and Ni contents in pyrite to their compositions in the mineralizing fluids (ESM 1). First, the partition dependence of Co and Ni between the hydrothermal fluid and coexisting pyrite with temperature have been estimated using Reaction B, C, and D, assuming that Fe, Co and Ni are transported primarily as chloride complexes (Fig. 9).

$$CoCl_2\ (aq) + FeS_2\ (s) \leftrightarrow CoS_2\ (s) + FeCl_2\ (aq) \quad (B)$$

$$NiCl_2\ (aq) + FeS_2\ (s) \leftrightarrow NiS_2\ (s) + FeCl_2\ (aq) \quad (C)$$

$$CoCl_2\ (aq) + NiS_2\ (s) \leftrightarrow CoS_2\ (s) + NiCl_2\ (aq) \quad (D)$$

Reactions B-D have been used to calculate Co/Fe, Ni/Fe, and Co/Ni for the hydrothermal fluids at Yulekenhalasu, using results of the fluid inclusion study of Wu (2018). As illustrated in Figures 9b and c, Ni and Co concentrations in pyrite appear to increase along with Ni/Fe and Co/Fe in the hydrothermal fluid. An increase in temperature will decrease Co contents and increase Ni contents in pyrite (Fig. 9b, c), causing Co/Ni in pyrite to increase with decreasing temperatures (Fig. 9d).

Discussion

Trace element substitution and correlations in pyrite

Trace elements can be incorporated into the pyrite crystal structure through stoichiometric lattice substitution, non-stoichiometric substitution, and as micro- or nano-inclusions (Huston et al., 1995; Keith et al., 2016; Keith et al., 2018; Large et al., 2014; Reich et al., 2013; Sykora et al., 2018). When observing time-resolved LA–ICP–MS spectra for pyrite (Fig. 10), Co and Ni concentrations are typically parallel to Fe concentrations, consistent with Co and Ni occurring within the pyrite crystal lattice and substituting for Fe in a stoichiometric manner (Huston et al., 1995). However, several pyrite analyses from Yulekenhalasu showed abrupt changes in signal intensity for Co or Ni in time-resolved depth profiles, indicating the presence of discrete growth zones of Co or Ni as stoichiometric lattice substitution in pyrite (Fig. 10a–c). Both As and Se are commonly present in measurable concentrations in pyrite and can substitute for S into the crystal lattice (Abraitis et al., 2004;

Zhou et al., 2010). Huston et al. (1995) concluded that As is incorporated into pyrite as a non-stoichiometric substitution, in contrast to Se that occurs as a stoichiometric substitution.

The abrupt changes in element counts for Cu, Pb, and Zn in the time-resolved spectra for some pyrite analyses (Fig. 10c, d) indicate the presence of nano- or micro-inclusions in pyrite; i.e., chalcopyrite and tetrahedrite-tennantite series inclusions for Cu, galena inclusions for Pb, and sphalerite inclusions for Zn (Huston et al., 1995; Large et al., 2014; Reich et al., 2013). Positive correlations of Bi with Cu, Pb and Ag (Fig. 11a–c) suggest the presence of Bi-rich or Bi-bearing tetrahedrite and galena (Abraitis et al., 2004). Gold shows a positive correlation with Bi and Te (Fig. 11e, f), but no correlation with As (Fig. 11g), highlighting a potential role for Bi and/or Te complexes in the transport of Au in magmatic-hydrothermal systems (Acosta-Góngora et al., 2015; Cook et al., 2009). Consequently, Au is most likely occurring as micro- or nano-inclusions of Au telluride or bismuthide in pyrite (Reich et al., 2013).

Paragenetic and spatial variation of trace elements in pyrite

A LA–ICP–MS element map of a composite pyrite grain that has a core of Py_{IIa} (potassic alteration) and a rim of Py_V (argillic alteration) is shown on Figure 12. The texture of Py_{IIa} is well preserved despite overprinting of Py_V, implying that the trace elements in Py_{IIa} have not been mobilized by subsequent alteration events. Elemental zoning in Py_{IIa} is interpreted to be related to contamination by silicates, based on the correlation between high Al contents and mineral inclusions in pyrite (Fig. 12b, c). As illustrated in Figure 9d, Co/Ni in hydrothermal fluid for Py_{IIa} (median of 20) is higher than for Py_V (median of 4). The lower Co/Ni values in Py_{IIa} (median of 0.2) than in Py_V (median of 10) is attributed to the higher crystallizing temperature of Py_{IIa} (~400 °C) compared to Py_V (~160 °C; Fig. 9d), because increasing temperatures would have negative affect on Co/Ni ratios in pyrite (Fig. 9d). The map highlights that Cu has lower concentrations in Py_V than Py_{IIa} (Fig. 12c). There are Au inclusions in Py_V (Fig. 12c), which may explain the presence of Au mineralization in argillic

460 altered rocks.

461 Fluids associated with sodic-calcic alteration (stage I) have similar Se/S compared to the
462 potassic stage, suggesting a similar origin for their hydrothermal fluids (Fig. 9a). The Se/S of
463 stage IV fluids broadly overlap with I and IIa (Fig. 9a), and are systematically higher than
464 those of stages IIb, III and V. These observations, combined with the involvement of meteoric
465 water in forming stage III, suggest that the hydrothermal fluid responsible for the stage IV
466 late Cu sulfide-bearing veins is similar to stages I and IIa and is also of magmatic-
467 hydrothermal origin.

468 Nickel and Co concentrations in pyrite appear to show significant variation across
469 different paragenetic stages (Fig. 11h). The hydrothermal fluids responsible for sodic-calcic
470 alteration were characterized by higher Co/Ni and Co/Fe but lower Ni/Fe than the potassic
471 stage fluids (Fig. 9b–d). The increase of Ni/Fe from sodic-calcic to potassic alteration could
472 be explained by a decrease of Fe caused by magnetite crystallization during potassic
473 alteration. The decline in Co/Fe during potassic alteration is possibly controlled by aqueous
474 dispersion of Co, considering the high solubility of Co chloride complexes in the fluid
475 compared to Ni (Acosta-Góngora et al., 2014; Liu et al., 2012). Higher Ni contents in pyrite
476 are typical in mafic host rocks (Bajwah et al., 1987; Botinelly et al., 1985), suggesting that
477 higher Ni/Fe in stage IV relative to stages I and IIa could be a result of hydrothermal fluids
478 derived from or interacting with a mafic source during stage IV (Zhao et al., 2011). This
479 mafic source may have been an intrusive analogue from regional Carboniferous units such as
480 the Jiangbasitao Formation and Heishantou Formation (Wang and Xu, 2006).

481 Pyrite from stages I and IIa, which formed at high temperature (Wu, 2018), are depleted
482 in most trace elements (Fig. 6), probably due to the slow growth rate for pyrite in high-
483 temperature environments which allows trace elements to be incorporated into other sulfide
484 phases rather than concentrated in pyrite (Large et al., 2009). Trace elements enriched in
485 pyrite from propylitic alteration are dominated by lithophile elements (e.g., Ti, Zr, Gd, Hf, and
486 Th), possibly reflecting their incorporation during the rapid growth of pyrite grains in the
487 lower-temperature environment(Large, 2011; Large et al., 2009; Melekestseva et al., 2014).

Lower-temperature conditions may have contributed to the enrichment of lithophile elements in Py_S (e.g., Zr, Hf, Th, Mo, W, and Tl; Fig. 6). This is because pyrite of sedimentary origin also tends to be contaminated by silicate micro-inclusions (e.g., silicate minerals that are more enriched in lithophile elements than pyrite) during the rapid growth of sulfides (Large et al., 2014). The enrichment of Cu, Bi, and Ag in stage IV pyrite implies deposition from a fertile metallogenic hydrothermal fluid (Melekestseva et al., 2014), which is consistent with the sulfide-rich mineral assemblages in stage IV veins. The remarkable enrichment of low-temperature distal pathfinder elements such as Te, Au and Tl in stage V pyrite is inferred to be related to a low temperature of formation, as indicated by the associated low-temperature (~160 °C) fluid inclusion assemblages and dark-cathodoluminescence quartz (Wu, 2018) in argillic alteration (Figs. 3, 5c).

Copper is concentrated in pyrite proximal to centers of mineralization at Yulekenhalasu (Fig. 9c-e; ESM 4b-n), implying that ore-forming fluid compositions are the critical factor in producing high concentrations of ore-forming elements in pyrite (Reich et al., 2013), although temperature and other factors cannot be excluded. High Au concentrations occur distal to the ore body in stage III pyrite (ESM 2q and 3s), and may suggest that Au precipitates further from the hydrothermal center than Cu. The spatial distribution pattern for Se in pyrite shows high concentrations close to the orebody in stages I (ESM 3h and 4j) and IIa (ESM 3i and 4k), but low concentrations close to orebody in stages IIb (ESM 3j and 4h) and III (ESM 3k and 4i). For stages I and IIa with temperatures above 300 °C, the curves in Figure 9a change to horizontal indicating that temperature has a negligible impact on the Se content in pyrite, whereas increased Se/S in the hydrothermal fluid from 3×10^{-7} to 1×10^{-6} could account for high Se in pyrite close to orebody (ESM 3h, 3i, 4j, and 4k). However, for stages IIb and III pyrite which formed below 300 °C (Wu, 2018), the corresponding curves in Figure 9a are steep, indicating temperature has a significant inverse effect on Se concentrations in pyrite formed during these stages. Lower Se concentrations in pyrite formed close to the orebody (ESM 4h and 4i) are possibly due to the relatively higher temperature present in the center of mineralization (Huston et al., 1995).

Genetic model

Porphyry-type alteration and mineralization

The intimate spatial relationship between Devonian diorite porphyry stocks and porphyry-type mineralization at Yulekenhalasu suggests a genetic link that is supported by geochronology (Wu et al., 2015; Yang et al., 2014). The hydrous syn-mineralization diorite porphyry was a product of magmatism triggered by flat subduction of the Paleo-Asian ocean plate beneath the Junggar arc (Wu et al., 2015). Flat subduction created thickened crust that formed the hydrous syn-mineralization magma (Loucks, 2014; Wu et al., 2015). The nature of low temperature (ca. 675 °C by Ti-in-zircon temperature) and high oxygen fugacity (FMQ + 3 by zircon oxybarometer) in ca. 377 Ma syn-mineralization magma (Wu et al., 2015), prevents the escape of chalcophile elements as sulfide and makes the diorite porphyry a favorable source for porphyry mineralization (Fig. 13a).

Combined with the mineral assemblages in stages I and IIa, the similar Se/S for the sodic-calcic and potassic stage fluids are consistent with fluids for both stages being derived from the diorite porphyry. Propylitic alteration spatially extends from the diorite porphyry into andesitic and basaltic wall rocks, recording the migration of hydrothermal fluids outwards from the locus of magmatic-hydrothermal activity (Fig. 4a; Cooke et al., 2014). Propylitic pyrite is enriched in lithophile elements (Fig. 6) due to rapid growth and assimilation of silicate phases at lower temperatures (~200 °C; Table 1). Phyllic alteration was superimposed onto early-formed porphyry-type alteration (Figs. 2a, 4g, h), with higher Ni/Fe in stage III compared to paragenetic stages I and IIa (Fig. 9c) interpreted to result from dispersion of Fe, indicated by the absence of magnetite or hematite (Fig. 3). The high Ni/Fe in propylitic alteration stage (Fig. 8c) suggests the interaction between hydrothermal fluids and basaltic wall rock which may have contributed more Ni than Fe to fluids.

Post-porphyry stage alteration and mineralization

Porphyry-type alteration at Yulekenhalasu was overprinted by stage IV Cu sulfide-bearing veins (Fig. 5a, b) and then by stage V argillic assemblages (Fig. 5d, e). Pyrite compositions, combined with microthermometric data (Table 1) and cathodoluminescence imaging (Wu, 2018), imply that late Cu sulfide-bearing veins (stage IV) were deposited at temperatures around 234–317 °C from CO_2-rich fluids, along with high concentrations of chalcophile elements.

The origin for stage IV mineralization could be attributed to 1) remobilization of preexisting mineralization for the porphyry deposit during orogenesis (e.g., Cairns et al., 2003; Li et al., 2012); 2) overprinting by a temporally discrete magmatic-hydrothermal system (e.g., Guo et al., 2011; Masterman et al., 2004; Masterman et al., 2005; Nie et al., 2004; Wu et al., 2018); or 3) superimposition of epithermal veins on a preexisting porphyry system (e.g., Cooke and Bloom, 1990; Li et al., 2015; Sillitoe, 1972). Based on the elemental data of pyrite collected from the Sarekuobu orogenic gold deposit in the Chinese Altay Orogen (Zheng et al., 2021), the estimated median values of Se/S of metamorphic fluids (3×10^{-8}) for orogenic gold deposit in this region is lower than Py_I ($\sim 3 \times 10^{-7}$) and Py_{IIa}, ($\sim 1 \times 10^{-6}$; Fig. 9a) from magmatic-hydrothermal fluids. Therefore, the higher Se/S of hydrothermal fluids for stage IV compared to those in orogenic gold systems, combined with the broad overlap of Se/S values for stage IV with magmatic-hydrothermal stages I and IIa pyrite, suggest a magmatic-hydrothermal origin, rather than orogenic (metamorphic) origin (Chen et al., 2007; Goldfarb et al., 2001). During the Late Devonian to Carboniferous, magmatism was widespread in the Chinese Altay–East Junggar (Chen et al., 2001; Han, 2008; Wan et al., 2011; Wu et al., 2015; Wu et al., 2019; Zhang et al., 2009). High Ni/Fe in pyrite for stage IV could be explained by an unexposed mafic intrusion source that formed in the island arc during the Late Devonian to Carboniferous at Yulekenhalasu (Fig. 13b), although the possibility of depletion of Fe, which is suggested by the absence of magnetite or hematite (Fig. 3), cannot be excluded. Having excluded the metamorphic and granitic origins for stage IV using pyrite compositions, combined with the fact that mafic magmas formed in island arc

settings are characterized by the higher CO_2 contents (1,246 mm^3/g) than those formed in other settings (Tang et al., 2017), the occurrence of CO_2-bearing fluid inclusions in late Cu sulfide-bearing veins suggests the mafic magma is the most likely origin based on current research. Meanwhile, it is unlikely that stage IV formed by the superimposition of epithermal fluids because of the CO_2-rich characteristics of the fluid inclusions, which imply deeper levels of formation than for the epithermal environment (Chen, 2010; Cooke and Simmons, 2000; Hedenquist et al., 1998).

The presence of pervasive argillic alteration (stage V) in the post-mineralization alkali granite porphyry (ca. 330 Ma) and continuous stringers of CL-dark quartz cutting across all the earlier quartz generations at Yulekenhalasu are indicators of a younger hydrothermal event (< 330 Ma) that produced argillic alteration (Wu, 2018). More importantly, this study has performed ^{40}Ar-^{39}Ar dating of sericite from the argillic alteration (stage V), yielding the weighted plateau age of 277.3 ± 1.3 Ma with two standard deviations (2σ; ESM 1 and 5). Moreover, Yang et al. (2013) performed ^{40}Ar–^{39}Ar dating on muscovite and biotite from the regional shear zone at Yulekenhalasu, yielding plateau ages of 283.8 ± 1.5 Ma and 277 ± 2 Ma, respectively, which are interpreted to constrain the deformation age. These ages are roughly coeval with regional deformation associated with the Erqis Fault at 297–261 Ma (Laurent-Charvet et al., 2003). A large number of orogenic Au deposits are distributed along second-order ductile fault zones within 5–10 km of the crustal-scale Erqis fault belt (Pirajno, 2013; Wan et al., 2011; Yang et al., 2018a), with their mineralization ages synchronous with the main time of movement of the Erqis Fault during 297-261 Ma, e.g., 292.9 ± 1 Ma for Duolanasayi and 289.2 ± 3.1 Ma for Saidu (Yang et al., 2018a). It is widely accepted that metamorphism caused by deformation generates ore-forming fluids, which extract Au from the wall rocks and migrate upward along the Erqis fault belt as conduits (Chen et al., 2001; Goldfarb et al., 2001; Sibson, 2004; Zheng et al., 2021). Gold is then deposited at the brittle-ductile boundary as a result of an acute change of pressure and oxygen fugacity (Cox et al., 2005; Sibson, 2004; Zheng et al., 2021). At Yulekenhalasu, stage V argillic alteration was

595 structurally controlled by shear zones and fractures (Figs. 2b, 5d, 12a). The mineral
596 assemblages in the argillic alteration zone are featured by fine-grained quartz, kaolinite,
597 muscovite, illite, calcite, and pyrite (Fig. 3), which is similar to those in orogenic Au deposits,
598 e.g., carbonates, quartz, muscovite, albite, pyrite, etc. (Chen et al., 2007; Goldfarb et al., 2001).
599 Note that kaolinite has also been reported in orogenic Au deposits in the Chinese Altay and
600 East Junggar region (Feng, 2019), with its formation mechanism explained by the reaction of
601 laumontite + CO_2 = kaolinite + calcite + quartz + H_2O (Bucher and Grapes, 2011; Wang et al.,
602 2019). Gold inclusions are present in stage V pyrite grains (Fig. 12c) and the highest Au
603 concentrations among all hydrothermal alteration stages were detected in Py_V (Fig. 6c),
604 implying that argillic alteration at Yulekenhalasu could be genetically linked to orogenic Au
605 mineralization in the Chinese Altay–East Junggar region during the Early Permian (Fig. 13c).
606 Besides, it's not surprising to observe superimposition of fluids derived from the Permian
607 orogenic Au mineralization on the Devonian porphyry Cu deposit, given the post-
608 mineralization burial at Yulekenhalasu in the Carboniferous (Wang and Xu, 2006).
609

610 ## Implications

611 Four porphyry-type alteration stages and two stages of overprinting alteration have been
612 identified at Yulekenhalasu, with porphyry-stage potassic and a superimposed late-stage Cu
613 sulfide-bearing vein event being the principal ore-forming stages. Se/S and Co/Ni in pyrite
614 increased with increasing Se/S and Co/Ni in the mineralizing hydrothermal fluids, but
615 decreased with increasing temperatures. A Devonian diorite porphyry was the source of
616 porphyry-style alteration and mineralization during stages I–III. Stage IV late Cu sulfide-
617 bearing veins overprinted the porphyry system in the Late Devonian-Carboniferous, possibly
618 related to an unexposed mafic intrusion. Argillic alteration was produced during regional
619 orogenic Au mineralization and strike-slip deformation in the Early Permian. Consequently,
620 ancient porphyry deposits formed in the Central Asian Orogenic Belt can be modified by
621 post-mineralization events than can cause hypogene upgrading and overprinting of barren
622 alteration assemblages, which can create challenges for mineral exploration, but also

opportunities for the formation of hybrid hypogene resources such as at Yulekenhalasu. This study indicates that more attention should be paid to the paragenesis study on porphyry Cu deposits in the world's ancient orogenic belts, where various forms of mineralization develop in the same ore district. Also, our study highlights using the compositions of pyrite, a widespread mineral in various hydrothermal deposits, as a potential vectoring tool in a variety of magmatic-hydrothermal systems, e.g., porphyry Cu deposit, epithermal deposit, orogenic Au deposit, polymetallic vein deposit, etc.

Acknowledgements

We sincerely thank Zhenjiang Liu from the No. 4 Brigade of the Xinjiang Geology, Mineral Exploration and Development Bureau for field support in the Halasu belt. We also thank Sarah Gilbert, and Ivan Belousov for their assistance with laboratory work and sample analysis at the ARC Research Hub for Transforming the Mining Value Chain, CODES, University of Tasmania, Australia. This study was financially supported by the National Key R&D Program of China (2022YFC2903301), National Natural Science Foundation of China (41921003, 41902089, 42230810), Science and Technology Planning of Guangdong Province, China (2020B1212060055) received by Prof. Huayong Chen and Dr. Chao Wu.

Figure captions

Fig. 1. (a) Regional tectonic map of the Central Asian Orogenic Belt (modified from Jahn et al., 2000). (b) Tectonic map of the Chinese Altay–East Junggar terrane (modified from Wan et al., 2014). (c) Geologic map of the southeastern Chinese Altay orogenic belt and northeastern Junggar block, NW China (modified from Zhang et al., 2009).

Fig. 2. (a) Alteration zoning on cross-section of exploration line 16 (Wu et al., 2019). (b) Simplified geological map of Yulekenhalasu, showing the spatial distribution of argillic alteration in the eastern and western mineralized zone (Modified from the No. 4 Geological Party of the Xinjiang Bureau of Geology and Mineral Exploration and

651 Development). (c) Photography of surface-exposed argillic alteration in the eastern
652 mineralized zone. (d) Sharp fault contact between phyllic alteration and argillic
653 alteration. Note that argillic alteration is generally structurally controlled.
654
655 Fig. 3. Mineral paragenesis for the Yulekenhalasu copper deposit.
656
657 Fig. 4. Representative photographs and photomicrographs of alteration and mineralization
658 assemblages from Yulekenhalasu. (a) Stage I sodic-calcic alteration with randomly
659 oriented magnetite and actinolite replacing igneous biotite (46°36'17.01" N,
660 90°1'50.90" E; drill hole ZK2005, 890 m depth). (b) Stage IIa potassic alteration
661 characterized by fine-grained K-feldspar and quartz altering plagioclase (46°36'15.69"
662 N, 90°1'39.43" E; drill hole ZK1204, 432 m depth). (c) Quartz veins in the potassic zone
663 containing molybdenite and biotite that has been chlorite-altered, as well as late fissure-
664 filled calcite veinlets (46°36'14.43" N, 90°1'57.86" E; drill hole ZK2403, 1140 m depth).
665 (d) Reflected-light photomicrographs of stage IIa chalcopyrite intergrown with euhedral
666 pyrite and biotite (46°36'15.69" N, 90°1'39.43" E; drill hole ZK1204, 432 m depth). (e)
667 Stage IIb epidote selectively replacing plagioclase phenocrysts with fine-grained calcite
668 and quartz (CPL; 46°36'6.33" N, 90°1'21.72" E; surface sample at elevation of 1543 m).
669 (f) Stage III phyllic alteration with wormy veinlets of chlorite and patches of pyrite
670 (46°36'14.12" N, 90°1'43.25" E; drill hole ZK1606, 680 m depth). (g) Stage III quartz
671 veins with muscovite and minor illite-dominated halos replacing secondary K-feldspar
672 (46°36'16.92" N, 90°1'30.78" E; drill hole ZK0405, 159 m depth). (h) Stage III fine-
673 grained muscovite and chlorite replacing primary plagioclase and biotite, and
674 secondary biotite (CPL; 46°36'15.69" N, 90°1'39.43" E; drill hole ZK1204, 442 m depth).
675 Abbreviations: Kfs = K-feldspar, Act = actinolite, Pl = plagioclase, Cal = calcite, Bt =
676 biotite, Chl = chlorite, Ep = epidote, Qz = quartz, Ccp = chalcopyrite, Py = pyrite, Mag =
677 magnetite, Mol = molybdenite. Note that the subscripts for Py represent the
678 corresponding paragenetic stage of pyrite.

679

680 Fig. 5. Representative photographs and photomicrographs of late stage and supergene
681 alteration and mineralization assemblages at Yulekenhalasu. (a) Stage IV sheeted veins
682 cutting potassic and propylitic altered rocks and containing quartz, epidote, K-feldspar,
683 bornite, pyrite, and chalcopyrite. The inset figure illustrates the field distributions of the
684 specimens (46°36'1.68" N, 90°1'31.36" E; surface sample at elevation of 1531 m). (b)
685 Stage IV chalcopyrite vein with euhedral pyrite grains that injected potassic altered
686 diorite porphyry (46°36'18.06" N, 90°1'47.01" E; drill hole ZK1607, 787 m depth). (c)
687 Stage V pyrite, anhydrite, and calcite occurring in a shear plane (46°36'14.43" N,
688 90°1'57.86" E; drill hole ZK2403, 1146 m depth). (d) Argillic alteration overprinting
689 potassic alteration, with sheeted pyrite veins produced by dextral shearing during stage
690 V and inset figure outlining internal tectonic stress (46°36'14.43" N, 90°1'57.86" E; drill
691 hole ZK2403, 1159 m depth). (e) Stage V showing pyrite veins with local relict of
692 magnetite inclusions, indicating that stage V overprinted potassic alteration
693 (46°36'14.43" N, 90°1'57.86" E; drill hole ZK2403, 1159 m depth). (f) Stage VI
694 supergene alteration with hematite and malachite present along fracture plane
695 (46°36'9.93" N, 90°1'30.54" E; surface sample at elevation of 1537 m). Abbreviations:
696 Kfs = K-feldspar, Chl = chlorite, Ep = epidote, Qz = quartz, illite = Ilt, Bt = biotite, Anh =
697 anhydrite, Ccp = chalcopyrite, Py = pyrite, Mag = magnetite, Bn = bornite, Hem =
698 hematite, Mlc = malachite, Sp = sphalerite.

699

700 Fig. 6. Comparative box plot of log-base-10-transformed trace elemental concentrations in
701 pyrite from sodic-calcic alteration (Py_I), potassic stage (Py_{IIa}), propylitic stage (Py_{IIb}),
702 phyllic stage (Py_{III}), late Cu sulfide-bearing veins (Py_{IV}), and argillic assemblages (Py_V).
703 Pathfinder elements are highlighted by yellow background. Note that data of Py_S from
704 the sedimentary rocks of Jiangbasitao Formation that uncontinuously overlay
705 Yulekenhalasu are included for comparison.

706

Fig. 7. Spatial variations of Cu, Co and Ni in pyrite in a serize of NE-SW cross-sections of Yulekenhalasu: Trace element contents for combined and individual paragenetic stages (Py_I to Py_{IV}). X-axis relates to sample location in drillcore. Grey shades represent the ore-body projected onto the longitudinal section.

Fig. 8 The schematic diagram for the quantitative method to evaluate the distances of sampling locations to the orebody (a) and spatial trends of Cu and Co in porphyry-type alteration stages (b-f).

Fig. 9. Correlations between trace element ratios in pyrite and estimated values in hydrothermal fluids as a function of temperature. The dash curves in each panel represent the hydrothermal fluids with constant elemental ratios labelled by overlapped numbers with yellow backgrounds. (a) Temperature dependence of Se/S in pyrite. Note that Se/S in pyrite increases with $m_{\sum Se}/m_{\sum S}$ of fluid but decreases with temperature. (b) Temperature dependence of Co/Fe in pyrite. (c) Temperature dependence of Ni/Fe in pyrite. (d) Temperature dependence of Co/Ni in pyrite. Corresponding hydrothermal $m_{\sum Se}/m_{\sum S}$ values are estimated based on the temperatures of ~410 °C for sodic-calcic alteration (Wu et al., 2019), ~400 °C for potassic alteration, ~200 °C for propylitic alteration, ~230 °C for phyllic alteration, ~300 °C for late Cu sulfide-bearing veins and ~160 °C for argillic alteration stages (Wu, 2018; Table 1).

Fig. 10. Representative time-resolved depth profiles, demonstrating concentrations (in counts per second) of S, Cr, Mn, Fe, Co, Ni, Cu, Zn, As, Se, Ag, Te, Pb, and Bi in pyrite samples from Yulekenhalasu. Note the stair-step pattern of Co and Ni reflecting chemical zoning.

Fig. 11. LA-ICP-MS analysis of pyrite from Yulekenhalasu. (a) Bi versus Cu, (b) Bi versus Pb,

(c) Bi versus Ag, (d) Cu versus Ag, (e) Au versus Bi, (f) Au versus Te, and (g) Au versus As. The log base 10 transformation has been applied to all data points. Fitting lines, calculated by the method of least squares with r^2 values, are provided for porphyry-style alteration, late Cu sulfide-bearing veins, argillic alteration, and all data, respectively. All data are listed in ESM 2.

Fig. 12. LA-ICP-MS image of potassic-stage pyrite grains (Py_{IIa}) overgrown by argillic-stage pyrite (Py_V). Inset figure (a) outlines the area of the specimens of Py_{IIa} with dextral shear deformation; (b) reflected-light image of pyrite grain consisting of the core of Py_{IIa} and the rim of Py_V; (c) LA-ICP-MS images for Al, Co, Ni, Cu, Au, and Bi.

Fig. 13. Metallogenic model for the formation of the Yulekenhalasu Cu deposit. (a) Flat subduction generated the diorite porphyry and related stage I–III alteration and mineralization at ca. 382–372 Ma. (b) Stage IV late Cu sulfide-bearing veins derived from fluids of a deep mafic intrusion (unexposed) overprint the porphyry system possibly during the Late Devonian or Carboniferous. (c) Early Permian post-collisional shearing and deformation led to stage V argillic alteration.

Table 1 Microthermometric data of fluid inclusion assemblages from quartz at Yulekenhalasu deposit (Wu, 2018).

References

Abraitis, P.K., Pattrick, R.A.D., and Vaughan, D.J. (2004) Variations in the compositional, textural and electrical properties of natural pyrite: a review. International Journal of Mineral Processing, 74(1), 41–59.

Acosta-Góngora, P., Gleeson, S.A., Samson, I.M., Ootes, L., and Corriveau, L. (2014) Trace element geochemistry of magnetite and its relationship to Cu-Bi-Co-Au-Ag-U-W mineralization in the Great Bear magmatic zone, NWT, Canada. Economic Geology, 109(7), 1901–1928.

Acosta-Góngora, P., Gleeson, S.A., Samson, I.M., Ootes, L., and Corriveau, L. (2015) Gold Refining by Bismuth Melts in the Iron Oxide-Dominated NICO Au-Co-Bi (±Cu±W) Deposit, NWT, Canada. Economic Geology, 110(2), 291-314.

Acosta-Góngora, P., Potter, E.G., Lawley, C.J.M., Petts, D., and Sparkes, G. (2022) Uraninite chemistry of the Central Mineral Belt, Labrador, Canada: Application of grain-scale unsupervised machine-learning. Journal of Geochemical Exploration, 233.

Arancibia, O.N., and Clark, A.H. (1996) Early magnetite-amphibole-plagioclase alteration-mineralization in the Island Copper porphyry copper-gold-molybdenum deposit, British

Columbia. Economic Geology, 91(2), 402–438.

Bajwah, Z.U., Seccombe, P.K., and Offler, R. (1987) Trace element distribution, Co:Ni ratios and genesis of the Big Cadia iron-copper deposit, New South Wales, Australia. Mineralium Deposita, 22(4), 292–300.

Botinelly, T., Siems, D.F., and Sanzolone, R.F. (1985) Trace elements in disseminated sulfides, magnetite, and massive sulfides, West Shasta District, California. Economic Geology, 80(8), 2196–2205.

Bralia, A., Sabatini, G., and Troja, F. (1979) A revaluation of the Co/Ni ratio in pyrite as geochemical tool in ore genesis problems. Mineralium Deposita, 14(3), 353–374.

Cairns, C.P., Mapleson, D.B., Bewsher, A.W., and McCuaig, T.C. (2003) Understanding the structural controls on arsenic mineralisation and ore distribution at the Miitel nickel mine, Widgiemooltha, Western Australia. Fifth International Mining Geology Conference, p. 61–72, Bendigo, Victoria.

Campbell, F.A., and Ethier, V.G. (1984) Nickel and cobalt in pyrrhotite and pyrite from the Faro and Sullivan orebodies. Canadian Mineralogist, 22(3), 503–506.

Carroll, A.R., Liang, Y.h., Graham, S.A., Xiao, X.C., Hendrix, M.S., Chu, J.C., and McKnight, C.L. (1990) Junggar basin, northwest China: trapped Late Paleozoic ocean. Tectonophysics, 181(1-4), 1–14.

Chen, H.Y., Chen, Y.J., and Liu, Y.L. (2001) Metallogenesis of the Ertix gold belt, Xinjiang and its relationship to Central Asia-type orogenesis. Science in China Series D-Earth Sciences, 44(3), 245–255.

Chen, Y.J. (2010) On epizonogenism and genetic classification of hydrothermal deposits. Earth Science Frontiers, 17, 27–34.

Chen, Y.J., Ni, P., Fan, H.R., F, P., Lai, Y., Su, W.C., and Zhang, H. (2007) Diagnostic fluid inclusions of different types hydrothermal gold deposits. Acta Petrologica Sinica, 23(9), 2085–2108.

Cook, N.J., Ciobanu, C.L., and Mao, J. (2009) Textural control on gold distribution in As-free pyrite from the Dongping, Huangtuliang and Hougou gold deposits, North China Craton (Hebei Province, China). Chemical Geology, 264(1–4), 101–121.

Cooke, D.R., Baker, M., Hollings, P., Sweet, G., Chang, Z., Danyushevsky, L., Gilbert, S., Zhou, T., White, N.C., and Gemmell, J.B. (2014) New advances in detecting the distal geochemical footprints of porphyry systems—epidote mineral chemistry as a tool for vectoring and fertility assessments. In K.D. Kelley, and H.C. Golden, Eds. Building Exploration Capability for the 21st Century, 18, p. 1–27. Society of Economic Geologists Special Publication.

Cooke, D.R., and Bloom, M.S. (1990) Epithermal and subjacent porphyry mineralization, Acupan, Baguio district, Philippines: a fluid-inclusion and paragenetic study. Journal of Geochemical Exploration, 35(1), 297–340.

Cooke, D.R., and Simmons, S.F. (2000) Characteristics and genesis of epithermal gold deposits. Reviews in Economic Geology, 13, 221–244.

Cox, S.F., Hedenquist, J.W., Thompson, J.F.H., Goldfarb, R.J., and Richards, J.P. (2005) Coupling between deformation, fluid pressures, and fluid flow in ore-producing hydrothermal systems at depth in the crust. One Hundredth Anniversary Volume, p. 0. Society of Economic Geologists.

D'yachkova, I.B., and Khodakovsky, I.L. (1968) Thermodynamic equilibria in the systems S-H_2O, Se-H_2O, and Te-H_2O in the 25-300 °C temperature range and their geochemical interpretations. Geochemistry International, 5, 1108–1125.

Danyushevsky, L., Robinson, P., Gilbert, S., Norman, M., Large, R., McGoldrick, P., and Shelley, M. (2011) Routine quantitative multi-element analysis of sulphide minerals by laser ablation ICP-MS: Standard development and consideration of matrix effects. Geochemistry: Exploration, Environment, Analysis, 11(1), 51–60.

Diener, A., Neumann, T., Kramar, U., and Schild, D. (2012) Structure of selenium incorporated in pyrite and mackinawite as determined by XAFS analyses. Journal of Contaminant Hydrology, 133, 30-39.

Du, S.J., Qu, X., Zhang, Y., Cheng, S.L., Lu, H., Wu, Q., and Xu, X. (2010) Chronology and tectonic setting of the intrusive bodies and associated porphyry copper deposit in Hersai area, eastern Junngar. Acta Petrologica Sinica, 26(10), 2981–2996.

Geng, X.X., Yang, F.Q., Zhang, Z.X., Liu, F., Chai, F.M., and Gao, G.J. (2013) Ore-forming fluid of Yulekenhalasu Cu-Mo deposit on the northern margin of Junggar basin, Xinjiang. Geological Review, 59(2), 235–247.

Goldfarb, R.J., Groves, D.I., and Gardoll, S. (2001) Orogenic gold and geologic time: a global synthesis. Ore Geology Reviews, 18(1-2), 1–75.

Guo, W.M., Lu, J.J., Zhang, R.Q., Zhao, Z.J., and Xu, Z.W. (2011) The superimposed mineralization of the Dongguashan Cu deposit in Tongling area, Anhui Province: evidence from the ore texture. Acta Geologica Sinica, 85, 1223–1232.

Han, B.F. (2008) A preliminary comparison of Mesozoic granitoids and rare metal deposits in Chinese and Russian Altai Mountains. Acta Petrologica Sinica, 24(4), 655–660.

Han, B.F., Ji, J.Q., Song, B., Chen, L.H., and Li, Z.H. (2004) SHRIMP zircon U-Pb ages of Kalatongke No. 1 and Huangshandong Cu-Ni-bearing mafic-ultramafic complexes, north Xinjiang, and geological implications. Chinese Science Bulletin, 49(22), 2424–2429.

Hawley, J.E., and Nichol, I. (1959) Selenium in some Canadian sulfides. Economic Geology, 54(4), 608–628.

Hedenquist, J.W., Arribas, A., and Reynolds, T.J. (1998) Evolution of an intrusion-centered hydrothermal system: Far Southeast-Lepanto porphyry and epithermal Cu-Au deposits, Philippines. Economic Geology, 93(4), 373–404.

Heinhorst, J., Lehmann, B., Ermolov, P., Serykh, V., and Zhurutin, S. (2000) Paleozoic crustal growth and metallogeny of Central Asia: evidence from magmatic-hydrothermal ore systems of Central Kazakhstan. Tectonophysics, 328(1), 69–87.

Hong, T., Dolejs, D., Zhai, M.G., Oscar, L., Xu, X.W., Gao, J., Schloglova, K.D., and Wang, Y.J. (2021a) Multiple tectonic-magmatic Mo-enrichment events in Yuleken porphyry Cu-Mo deposit, NW China and its' implications for the formation of giant porphyry Mo deposit. Ore Geology Reviews, 139.

Hong, T., Hollings, P., Zhai, M.-G., Wang, Y.-X., Xu, X.-W., Gao, J., and Wang, Y.-J. (2021b) Superimposed mineralization in the deformed Yulekenhalasu porphyry Cu-Mo deposit (Northwest China): Rb-Sr geochronology, S isotope, and trace element analysis of chalcopyrite. Ore Geology Reviews, 135, 104226.

Hong, T., Klemd, R., Gao, J., Xiang, P., Xu, X.W., You, J., Wang, X.S., Wu, C., Li, H., and Ke, Q. (2017) The tectonic evolution of the Irtysh tectonic belt: New zircon U-Pb ages of arc-related and collisional granitoids in the Kalaxiangar tectonic belt, NW China. Lithos, 272, 46-68.

Hong, T., Xu, X.-W., Gao, J., Peters, S.G., Li, J., Cao, M., Xiang, P., Wu, C., and You, J. (2018) Element migration of pyrites during ductile deformation of the Yuleken porphyry Cu deposit (NW-China). Ore Geology Reviews, 100, 205-219.

Huston, D.L., Sie, S.H., Suter, G.F., Cooke, D.R., and Both, R.A. (1995) Trace elements in sulfide minerals from eastern Australian volcanic-hosted massive sulfide deposits; Part I, Proton microprobe analyses of pyrite, chalcopyrite, and sphalerite, and Part II, Selenium levels in pyrite; comparison with delta ^{34}S values and implications for the source of sulfur in volcanogenic hydrothermal systems. Economic Geology, 90(5), 1167–1196.

Jahn, B.M. (2004) The Central Asian Orogenic Belt and growth of the continental crust in the Phanerozoic. Geological Society, London, Special Publications, 226(1), 73–100.

Jahn, B.M., Wu, F.Y., and Chen, B. (2000) Granitoids of the Central Asian Orogenic Belt and continental growth in the Phanerozoic. Geological Society of America Special Papers, 350, 181–193.

Keith, M., Hackel, F., Haase, K.M., Schwarz-Schampera, U., and Klemd, R. (2016) Trace element systematics of pyrite from submarine hydrothermal vents. Ore Geology Reviews, 72, 728-745.

Keith, M., Smith, D.J., Jenkin, G.R.T., Holwell, D.A., and Dye, M.D. (2018) A review of Te and Se systematics in hydrothermal pyrite from precious metal deposits: Insights into ore-forming processes. Ore Geology Reviews, 96, 269-282.

Large, R. (2011) A Carbonaceous sedimentary source-rock model for Carlin-type and orogenic gold deposits. Economic Geology, 106(3), 331–358.

Large, R.R., Danyushevsky, L., Hollit, C., Maslennikov, V., Meffre, S., Gilbert, S., Bull, S., Scott, R., Emsbo, P., and Thomas, H. (2009) Gold and trace element zonation in pyrite using a laser imaging technique: implications for the timing of gold in orogenic and Carlin-style sediment-hosted deposits. Economic Geology, 104(5), 635–668.

Large, R.R., Halpin, J.A., Danyushevsky, L.V., Maslennikov, V.V., Bull, S.W., Long, J.A., Gregory, D.D., Lounejeva, E., Lyons, T.W., and Sack, P.J. (2014) Trace element content of sedimentary pyrite as a new proxy for deep-time ocean–atmosphere evolution. Earth and Planetary Science Letters, 389, 209–220.

Laurent-Charvet, S., Charvet, J., Monié, P., and Shu, L.s. (2003) Late Paleozoic strike–slip shear zones in eastern Central Asia (NW China): New structural and geochronological data. Tectonics, 22(2), 1–24.

Layton-Matthews, D., Peter, J.M., Scott, S.D., and Leybourne, M.I. (2008) Distribution, mineralogy, and geochemistry of selenium in felsic volcanic-hosted massive sulfide deposits of the

Finlayson Lake district, Yukon Territory, Canada. Economic Geology, 103(1), 61–88.

Li, G.M., Zhang, X.N., Qin, K.Z., Sun, X.G., Zhao, J.X., Yin, X.B., Li, J.X., and Yuan, H.S. (2015) The telescoped porphyry-high sulfidation epithermal Cu(-Au) mineralization of Rongna deposit in Duolong ore cluster at the southern margin of Qiangtang Terrane, Central Tibet: Integrated evidence from geology, hydrothermal alteration and sulfide assemblages. Acta Petrologica Sinica, 31, 2307–2324.

Li, Q., Zhang, Z.X., Geng, X.X., Li, C., Liu, F., Chai, F.M., and Yang, F.Q. (2014) Geology and geochemistry of the Qiaoxiahala Fe–Cu–Au deposit, Junggar region, northwest China. Ore Geology Reviews, 57, 462–481.

Li, W.B., Zhong, R.C., Xu, C., Song, B., and Qu, W.J. (2012) U–Pb and Re–Os geochronology of the Bainaimiao Cu–Mo–Au deposit, on the northern margin of the North China Craton, Central Asia Orogenic Belt: Implications for ore genesis and geodynamic setting. Ore Geology Reviews, 48, 139–150.

Liu, G.R., Dong, L.H., Xue, C.J., Li, X.R., Zhang, L.W., Wei, G.Z., He, L.X., Zhao, Z.H., Qin, J.H., and Zhang, Z.X. (2010) Geological characteristics and exploration direction of the Yulekenhalasu copper deposit, Xinjiang. Xinjiang Geology, 28(4), 377–384.

Liu, T.G., Yu, X.Y., and Mei, H.J. (1991) The Duolanasayi-Kalaxiange'er porphyry copper-gold metallogenic belt. Geology and Geochemistry, 2, 71–74.

Liu, W.h., Migdisov, A., and Williams-Jones, A. (2012) The stability of aqueous nickel (II) chloride complexes in hydrothermal solutions: Results of UV–Visible spectroscopic experiments. Geochimica et Cosmochimica Acta, 94, 276–290.

Loftus-Hills, G., and Solomon, M. (1967) Cobalt, nickel and selenium in sulphides as indicators of ore genesis. Mineralium Deposita, 2(3), 228–242.

Long, L.L., Wang, Y.W., Du, A.D., Wang, J.B., Wang, L.J., Wang, S.L., Pu, K.X., and Qu, W.J. (2011) Molybdenite Re–Os age of Xilekuduke Cu–Mo deposit in Xinjiang and its geological significance. Mineral Deposits, 30(4), 635–644.

Lorand, J.-P., Alard, O., Luguet, A., and Keays, R.R. (2003) Sulfur and selenium systematics of the subcontinental lithospheric mantle: inferences from the Massif Central xenolith suite (France). Geochimica et Cosmochimica Acta, 67(21), 4137–4151.

Loucks, R.R. (2014) Distinctive composition of copper-ore-forming arcmagmas. Journal of the Geological Society of Australia, 61(1), 5–16.

Mao, J.W., Pirajno, F., Lehmann, B., Luo, M.C., and Berzina, A. (2014) Distribution of porphyry deposits in the Eurasian continent and their corresponding tectonic settings. Journal of Asian Earth Sciences, 79, 576–584.

Masterman, G.J., Cooke, D.R., Berry, R.F., Clark, A.H., Archibald, D.A., Mathur, R., Walshe, J.L., and Duran, M. (2004) $^{40}Ar/^{39}Ar$ and Re-Os geochronology of porphyry copper- molybdenum deposits and related copper-silver veins in the Collahuasi District, northern Chile. Economic Geology and the Bulletin of the Society of Economic Geologists, 99(4), 673-690.

Masterman, G.J., Cooke, D.R., Berry, R.F., Walshe, J.L., Lee, A.W., and Clark, A.H. (2005) Fluid chemistry, structural setting, and emplacement history of the Rosario Cu-Mo porphyry and Cu-Ag-Au epithermal veins, Collahuasi district, northern Chile. Economic Geology, 100(5), 835–862.

Melekestseva, I.Y., Tret'yakov, G.A., Nimis, P., Yuminov, A.M., Maslennikov, V.V., Maslennikova, S.P., Kotlyarov, V.A., Beltenev, V.E., Danyushevsky, L.V., and Large, R. (2014) Barite-rich massive sulfides from the Semenov-1 hydrothermal field (Mid-Atlantic Ridge, 13°30.87′ N): evidence for phase separation and magmatic input. Marine Geology, 349, 37–54.

Mossakovsky, A.A., Ruzhentsev, S.V., Samygin, S.G., and Kheraskova, T.N. (1994) Central Asian fold belt: geodynamic evolution and formation history. Geotectonics, 27(6), 445–474.

Nie, F.J., Jiang, S.H., Zhang, Y., Liu, Y., and Hu, P. (2004) Geological features and origin of porphyry copper deposits in China-Mongolia border region and its neighboring areas. Journal of Asian Earth Sciences, 23, 176–189.

Niu, L., Hong, T., Xu, X.W., Li, H., Ke, Q., Wang, X.H., and Ma, Y.C. (2020) A revised stratigraphic and tectonic framework for the Ashele volcanogenic massive sulfide deposit in the southern Chinese Altay: Evidence from stratigraphic relationships and zircon geochronology. Ore Geology Reviews, 127.

Perelló, J., Cox, D., Garamjav, D., Sanjdorj, S., Diakov, S., Schissel, D., Munkhbat, T.-O., and Oyun, G. (2001) Oyu Tolgoi, Mongolia: Siluro-Devonian porphyry Cu-Au-(Mo) and high-sulfidation Cu mineralization with a Cretaceous chalcocite blanket. Economic Geology, 96(6), 1407–1428.

Pirajno, F. (2013) The Geology and Tectonic Settings of China's Mineral Deposits. 909-910 p. Springer

950 Netherlands.
951 Qin, K.Z., Zhang, L.C., Ding, K.S., Xu, Y.X., Tang, D.M., Xu, X.W., Ma, T.L., and Li, G.M. (2009)
952 Mineralization type, Petrogenesis of ore-bearing intrusions and mineralogical characteristics
953 of Sanchakou copper deposits in eastern Tianshan. Acta Petrologica Sinica, 25(4), 845-861.
954 Reich, M., Deditius, A., Chryssoulis, S., Li, J.W., Ma, C.Q., Parada, M.A., Barra, F., and Mittermayr, F.
955 (2013) Pyrite as a record of hydrothermal fluid evolution in a porphyry copper system: A
956 SIMS/EMPA trace element study. Geochimica et Cosmochimica Acta, 104, 42–62.
957 Seltmann, R., Porter, T.M., and Pirajno, F. (2014) Geodynamics and metallogeny of the central
958 Eurasian porphyry and related epithermal mineral systems: a review. Journal of Asian Earth
959 Sciences, 79, 810–841.
960 Sengör, A.M.C., Natal'In, B.A., and Burtman, V.S. (1993) Evolution of the Altaid tectonic collage and
961 Palaeozoic crustal growth in Eurasia. Nature, 364(6435), 299–307.
962 Sibson, R.H. (2004) Controls on maximum fluid overpressure defining conditions for mesozonal
963 mineralisation. Journal of Structural Geology, 26(6-7), 1127-1136.
964 Sillitoe, R.H. (1972) A plate tectonic model for the origin of porphyry copper deposits. Economic
965 Geology, 67(2), 184–197.
966 Sillitoe, R.H. (2010) Porphyry copper systems. Economic Geology, 105(1), 3–41.
967 Sykora, S., Cooke, D.R., Meffre, S., Stephanov, A.S., Gardner, K., Scott, R., Selley, D., and Harris,
968 A.C. (2018) Evolution of pyrite trace element compositions from porphyry-style and
969 epithermal conditions at the Lihir gold deposit: Implications for ore genesis and mineral
970 processing. Economic Geology, 113(1), 193–208.
971 Tang, Q., Zhang, M., Feng, P., Wang, Y., Sun, F., Dang, Y., Wang, X., and Hu, F. (2017) The chemical
972 compositions and environmental implications of Carbonaceous volatile species of the mafic
973 magmatism in different tectonic settings. Bulletin of Mineralogy, Petrology and Geochemistry,
974 36(2), 237-244.
975 Tischendorf, G. (1966) Zur verteilung des selens in sulfiden. Freiberger Forschungshefte, 208, 1–162.
976 Wan, B., Xiao, W.J., Han, C.M., Windley, B.F., Zhang, L.C., Qu, W.J., and Du, A.D. (2014) Re–Os
977 molybdenite age of the Cu–Mo skarn ore deposit at Suoerkuduke in East Junggar, NW China
978 and its geological significance. Ore Geology Reviews, 56, 541–548.
979 Wan, B., Xiao, W.J., Windley, B.F., Gao, J., Zhang, L.C., and Cai, K. (2017) Contrasting ore styles and
980 their role in understanding the evolution of the Altaids. Ore Geology Reviews, 80, 910–922.
981 Wan, B., Xiao, W.J., Zhang, L.C., Windley, B.F., Han, C.M., and Quinn, C.D. (2011) Contrasting styles
982 of mineralization in the Chinese Altai and East Junggar, NW China: implications for the
983 accretionary history of the southern Altaids. Journal of the Geological Society, 168(6), 1311–
984 1321.
985 Wang, J.B., and Xu, X. (2006) Post-collisional tectonic evolution and metallogenesis in northern
986 Xinjiang, China. Acta Geologica Sinica, 80(1), 23–31.
987 Wang, T., Tong, Y., Li, S., Zhang, J.J., Shi, X.J., Li, J.Y., Han, B.F., and Hong, D.W. (2010) Spatial and
988 temporal variations of granitoids in the Altay orogen and their implications for tectonic setting
989 and crustal growth: perspectives from Chinese Altay. Acta Petrologica et Mineralogica, 29(6),
990 595–618.
991 Wang, Y.F., Chen, H.Y., Baker, M.J., Han, J.S., Xiao, B., Yang, J.T., and Jourdan, F. (2019) Multiple
992 mineralization events of the Paleozoic Tuwu porphyry copper deposit, Eastern Tianshan:
993 evidence from geology, fluid inclusions, sulfur isotopes, and geochronology. Mineralium
994 Deposita, 54(7), 1053-1076.
995 Wang, Y.F., Chen, H.Y., Falloon, T.J., and Han, J.S. (2022) The Paleozoic-Mesozoic magmatic
996 evolution of the Eastern Tianshan, NW China: Constraints from geochronology and
997 geochemistry of the Sanchakou intrusive complex. Gondwana Research, 103, 1-22.
998 Wang, Y.F., Chen, H.Y., Han, J.S., Chen, S.B., Huang, B.Q., Li, C., Tian, Q.L., Wang, C., Wu, J.X., and
999 Chen, M.X. (2018) Paleozoic tectonic evolution of the Dananhu-Tousuquan island arc belt,
1000 Eastern Tianshan: Constraints from the magmatism of the Yuhai porphyry Cu deposit,
1001 Xinjiang, NW China. Journal of Asian Earth Sciences, 153, 282–306.
1002 Windley, B.F., Kröner, A., Guo, J.H., Qu, G.S., Li, Y.Y., and Zhang, C. (2002) Neoproterozoic to
1003 Paleozoic geology of the Altai orogen, NW China: new zircon age data and tectonic evolution.
1004 The Journal of Geology, 110(6), 719–737.
1005 Wohlgemuth-Ueberwasser, C.C., Viljoen, F., Petersen, S., and Vorster, C. (2015) Distribution and
1006 solubility limits of trace elements in hydrothermal black smoker sulfides: An in-situ LA-ICP-
1007 MS study. Geochimica et Cosmochimica Acta, 159, 16–41.
1008 Wu, C. (2018) Magmatic evolution and multiphase superimposing mineralization in the Halasu Cu
1009 belt, Xinjiang. Guangzhou Institute of Geochemistry, Ph.D., p. 186. Chinese Academy of

Sciences.

Wu, C., Chen, H.Y., Hollings, P., Xu, D.R., Liang, P., Han, J.S., Xiao, B., Cai, K.D., Liu, Z.J., and Qi, Y.K. (2015) Magmatic sequences in the Halasu Cu Belt, NW China: Trigger for the Paleozoic porphyry Cu mineralization in the Chinese Altay-East Junggar. Ore Geology Reviews, 71, 373–404.

Wu, C., Chen, H.Y., Hong, W., Li, D.F., Liang, P., Fang, J., Zhang, L.J., and Lai, C. (2019) Magnetite chemistry and implications for the magmatic-hydrothermal ore-forming process: An example from the Devonian Yuleken porphyry Cu system, NW China. Chemical Geology, 522, 1-15.

Wu, C., Chen, H.Y., Liang, P., Han, J.S., Liu, Z.J., Fang, J., and Xu, D.R. (2018) Paragenesis and fluid evolution of the Halasu III porphyry Cu deposit, East Junggar (NW China): Implications for the Paleozoic multiphase superimposing mineralization in the Central Asian Orogenic Belt. Ore Geology Reviews, 100, 183–204.

Xiang, P. (2013) Geological characteristics, metallogenic epoch and its evolution process of the superimposed and tectonic reworked porphyry Cu–Mo deposits in the Kalaxianger porphyry copper ore belt, eastern Junggar. Beijing, China, Chinese University of Geosciences, PhD, p. 187. Chinese University of Geosciences (Beijing), Beijing, China.

Xiang, P., Zhang, L.C., Xu, X.W., Liu, G.R., Liu, Z.J., Jin, X.D., and Li, W.J. (2012) Geological characteristics and genesis of Yuleken-Halasu superimposed and tectonically reworked porphyry copper-gold (molybdenum) deposit in Qinghe, Xinjiang. Acta Petrologica Sinica, 28(8), 2369–2380.

Xiao, B., Chen, H.Y., Hollings, P., Han, J.S., Wang, Y.F., Yang, J.T., and Cai, K. (2017) Magmatic evolution of the Tuwu-Yandong porphyry Cu belt, NW China: Constraints from geochronology, geochemistry and Sr-Nd-Hf isotopes. Gondwana Research, 43, 74-91.

Xiao, W.J., Windley, B.F., Huang, B.C., Han, C.M., Yuan, C., Chen, H.L., Sun, M., Sun, S., and Li, J.L. (2009a) End-Permian to mid-Triassic termination of the accretionary processes of the southern Altaids: implications for the geodynamic evolution, Phanerozoic continental growth, and metallogeny of Central Asia. International Journal of Earth Sciences, 98(6), 1189–1217.

Xiao, W.J., Windley, B.F., Yuan, C., Sun, M., Han, C.M., Lin, S.F., Chen, H.L., Yan, Q.R., Liu, D.Y., and Qin, K.Z. (2009b) Paleozoic multiple subduction-accretion processes of the southern Altaids. American Journal of Science, 309(3), 221–270.

Xue, C.J., Chi, G.X., Zhao, X.B., Wu, G.G., Zhao, Z.F., and Dong, L.H. (2016) Multiple and prolonged porphyry Cu–Au mineralization and alteration events in the Halasu deposit, Chinese Altai, Xinjiang, northwestern China. Geoscience Frontiers, 7, 799–809.

Yakubchuk, A. (2004) Architecture and mineral deposit settings of the Altaid orogenic collage: a revised model. Journal of Asian Earth Sciences, 23(5), 761–779.

Yakubchuk, A., Degtyarev, K., Maslennikov, V., Wurst, A., Stekhin, A., and Lobanov, K. (2012) Tectonomagmatic settings, architecture, and metallogeny of the Central Asian copper province. Society of Economic Geologists, Special Publication, 16, 403–432.

Yamamoto, M. (1976) Relationship between Se/S and sulfur isotope ratios of hydrothermal sulfide minerals. Mineralium Deposita, 11(2), 197–209.

Yan, S.H., Teng, R.L., Zhang, Z.C., Chen, B.L., Chen, W., Zhou, G., and He, L.X. (2006) New understanding on origin of Kalaxiangeer copper deposit on southern margin of Altay mountain, Xinjiang: Constraints from S-Pb-H-O isotope geochemistry and ^{40}Ar-^{39}Ar age of Halasu copper deposit. Mineral Deposits, 25(3), 292–301.

Yang, F.Q., Chai, F.M., Zhang, Z.X., Geng, X.X., and Li, Q. (2014) Zircon U–Pb geochronology, geochemistry, and Sr–Nd–Hf isotopes of granitoids in the Yulekenhalasu copper ore district, northern Junggar, China: Petrogenesis and tectonic implications. Lithos, 190, 85–103.

Yang, F.Q., Geng, X.X., Wang, R., Zhang, Z.X., and Guo, X.J. (2018a) A synthesis of mineralization styles and geodynamic settings of the Paleozoic and Mesozoic metallic ore deposits in the Altay Mountains, NW China. Journal of Asian Earth Sciences, 159, 233-258.

Yang, F.Q., Li, Q., Yang, C.D., and Zhang, Z.X. (2018b) A combined fluid inclusion and S-H-O-He-Ar isotope study of the Devonian Ashele VMS-type copper-zinc deposit in the Altay orogenic belt, northwest China. Journal of Asian Earth Sciences, 161, 139-163.

Yang, F.Q., Liu, G.R., Qin, J.H., Zhang, Z.X., Liu, Z.J., Zhang, L.W., Wei, G.Z., Liu, F., and Geng, X.X. (2012) Fluid inclusion and stable isotope study of Yulekenhalasu copper-(molybdenum) deposit in northern margin of Junggar, Xinjiang. Mineral Deposits, 31, 965–982.

Yang, F.Q., Qin, J.H., Liu, F., Zhang, Z.X., Liu, Z.J., Geng, X.X., Chai, F.M., and Gao, W.J. (2013) Ar-Ar dating of the ductile shear zones in the Yulekenhalasu Cu-(Mo) ore deposit. Geotectonica et Metallogenia, 37, 1–10.

Zhang, Z.C., Zhou, G., Kusky, T.M., Yan, S.H., Chen, B.L., and Zhao, L. (2009) Late Paleozoic

volcanic record of the Eastern Junggar terrane, Xinjiang, Northwestern China: major and trace element characteristics, Sr–Nd isotopic systematics and implications for tectonic evolution. Gondwana Research, 16(2), 201–215.

Zhao, H.-X., Frimmel, H.E., Jiang, S.-Y., and Dai, B.-Z. (2011) LA-ICP-MS trace element analysis of pyrite from the Xiaoqinling gold district, China: Implications for ore genesis. Ore Geology Reviews, 43(1), 142-153.

Zhao, Y.M., Bi, C.S., Zou, X.Q., Sun, Y.L., Du, A.D., and Zhao, Y.M. (1997) The Re-Os isotopic age of molybdenite from Duobaoshan and Tongshan porphyry copper (molybdenite) deposits. Acta Petrologica Sinica, 18, 61–67.

Zheng, Y., Wu, Y.H., Yu, P.P., Hu, Z.B., and Chen, Y.J. (2021) Gold accumulation in the metavolcanic-hosted orogenic gold deposit constrained by pyrite paragenesis coupled with in-situ trace elements and sulfur isotope: The Sarekuobu example in the Chinese Altay Orogen. Ore Geology Reviews, 138.

Zhou, T.F., Zhang, L.J., Yuan, F., Fan, Y., and Cooke, D.R. (2010) LA-ICP-MS in situ trace element analysis of pyrite from the Xinqiao Cu-Au-S deposit in Tongling, Anhui, and its constraints on the ore genesis. Earth Science Frontier, 17(2), 306–319.

Table 1 Microthermometric data of FIAs from quartz at Yulekenhalasu deposit (Wu, 201

Alteration stage	Occurence[a]	Size (μm)	Filling (%)	Type[b]	No. of FIAs	Tm_{H2O} (°C)[c]		
						Min	Max	Mean
IIa potassic alteration	GZ, HF, I	3 to 13	30 to 40	A, B, C	18	-10.3	-1.2	-5.1
IIb propylitic alteration	GZ, HF	6	40	A, B	12	-12.7	-1.1	-5.5
III phyllic alteration	HF, I, S	3 to 9	10 to 30	A, B	10	-8.1	-1.9	-4.1
IV late Cu sulfide-bearing veins	GZ, HF, S	3 to 12	10 to 60	B, D	32	-6.4	-1.8	-4.6
V argillic alteration	HF, S, C	3 to 20	10 to 60	A, B	77	-12.9	-0.2	-4.4

[a]Occurence: GZ=Growth Zone, HF=Healing Fracture, RD=Randomly Distributed, I=Isolated, S=Scatter, C=

[b]Type: A=single-phase, B=liquid-vapor two-phase, C=liquid-vapor-solid three phase, D=CO2-bearing.

[c]Tm_{H2O}=final melting temperature of ice.

[d]Th-total = total homogenization temperature.

B)

Th-total (°C)[d]			Salinity (wt % NaCl)			Comments
Min	Max	Mean	Min	Max	Mean	
288.0	461.0	400.0	2.1	30.0	10.3	
164.0	336.0	200.0	1.9	16.6	8.0	
200.0	387.0	230.0	3.2	11.8	6.5	
234.0	317.0	300.0	1.0	17.4	8.5	CO2-bearing
100.0	252.0	160.0	0.4	16.8	6.7	

=Cluster.

Fig. 1

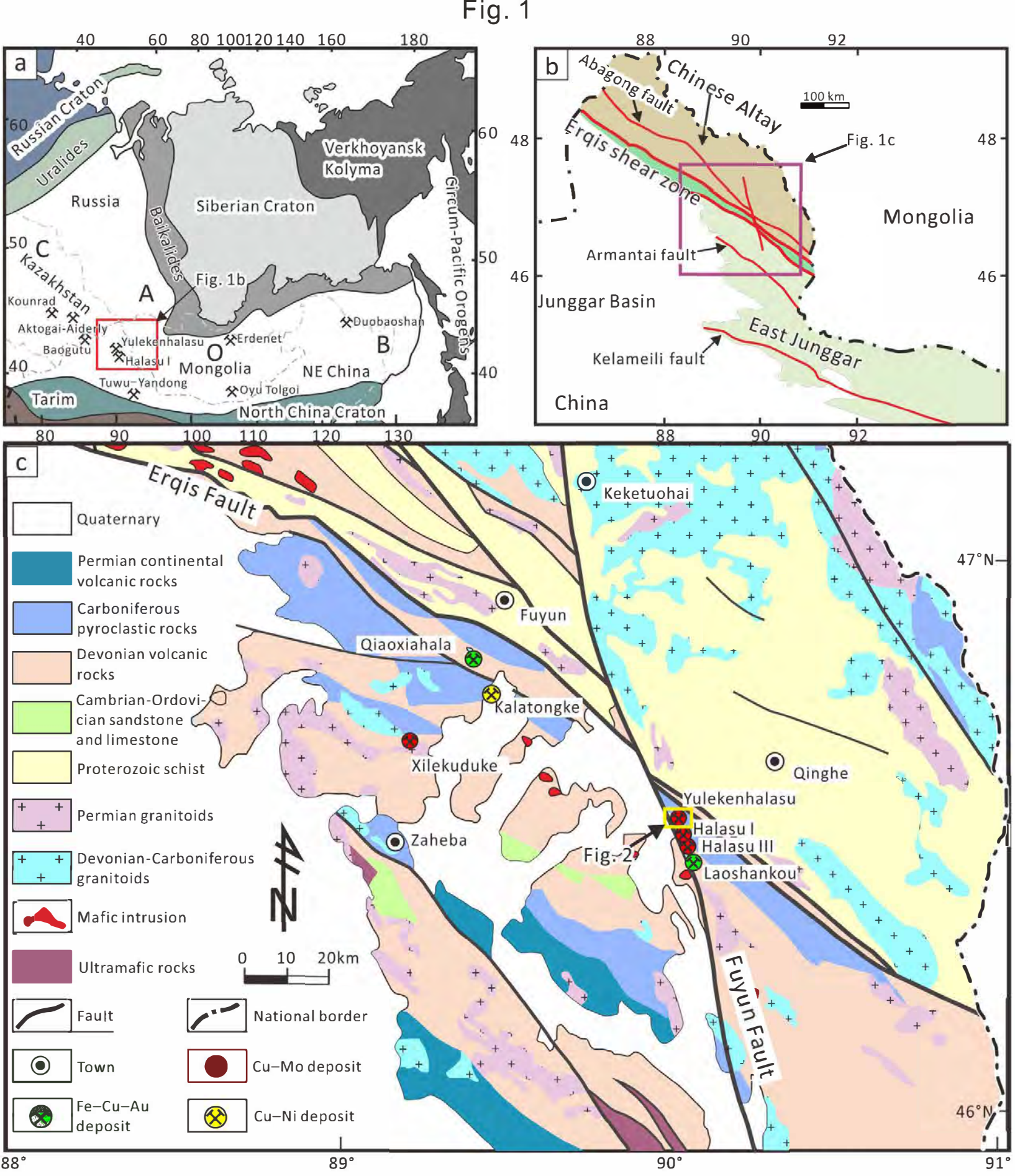
a
Russian Craton
Uralides
Russia
Verkhoyansk
Kolyma
Siberian Craton
Baikalides
Circum-Pacific Orogens
Kazakhstan
Fig. 1b
Kounrad
Aktogai-Aiderly
Baogutu
Yulekenhalasu
Halasu I
Erdenet
Duobaoshan
Mongolia
NE China
Tuwu–Yandong
Oyu Tolgoi
Tarim
North China Craton
b
Abagong fault
Chinese Altay
100 km
Fig. 1c
Erqis shear zone
Mongolia
Armantai fault
Junggar Basin
East Junggar
Kelameili fault
China
c
Erqis Fault
Quaternary
Permian continental volcanic rocks
Carboniferous pyroclastic rocks
Devonian volcanic rocks
Cambrian-Ordovician sandstone and limestone
Proterozoic schist
Permian granitoids
Devonian-Carboniferous granitoids
Mafic intrusion
Ultramafic rocks
Fault
National border
Town
Cu–Mo deposit
Fe–Cu–Au deposit
Cu–Ni deposit
Keketuohai
Fuyun
Qiaoxiahala
Kalatongke
Xilekuduke
Qinghe
Yulekenhalasu
Halasu I
Halasu III
Laoshankou
Zaheba
Fig. 2
Fuyun Fault
0 10 20km
47°N
46°N
88°
89°
90°
91°

Fig. 2

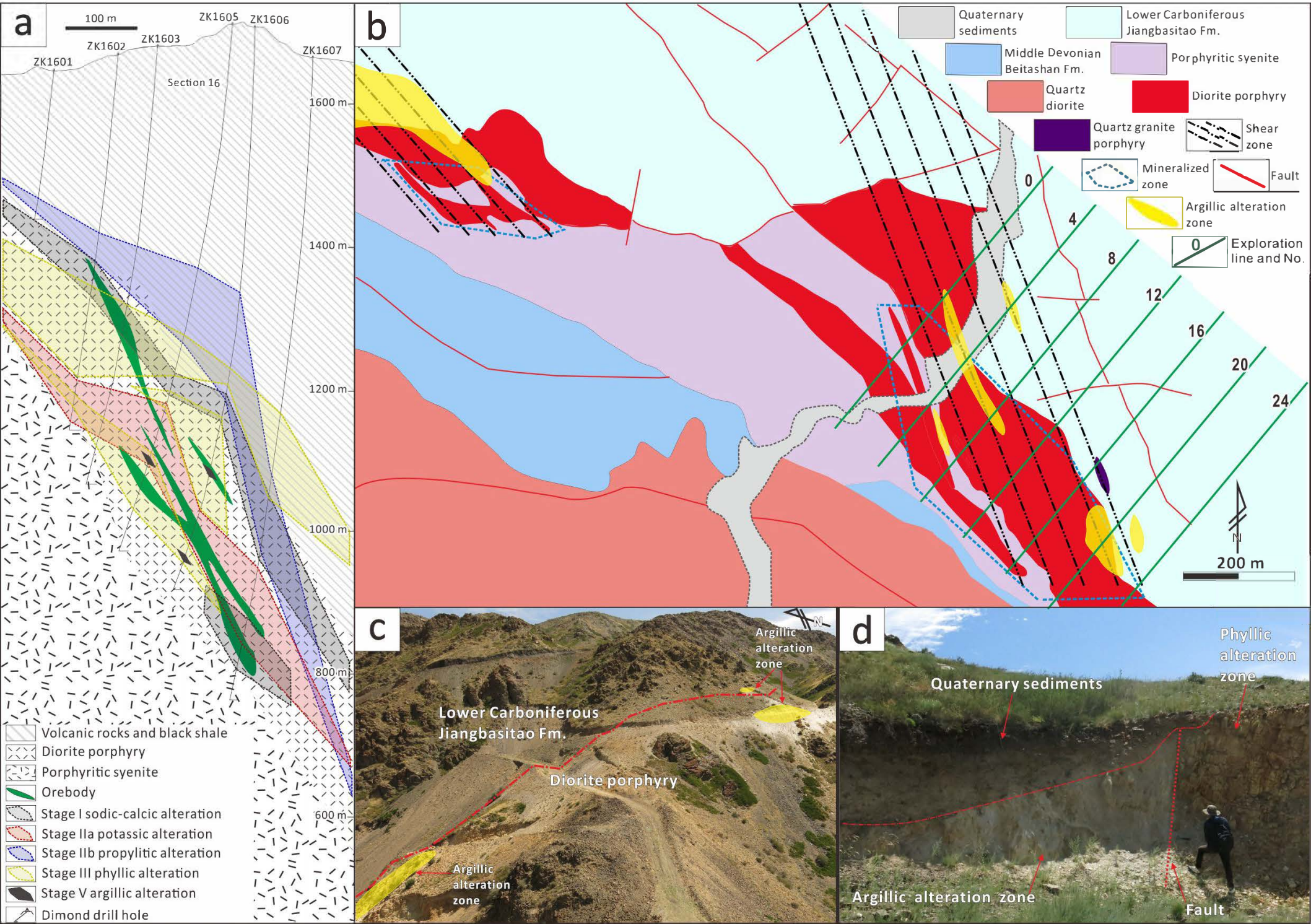
a
100 m
ZK1601
ZK1602
ZK1603
ZK1605
ZK1606
ZK1607
Section 16
1600 m
1400 m
1200 m
1000 m
800 m
600 m
Volcanic rocks and black shale
Diorite porphyry
Porphyritic syenite
Orebody
Stage I sodic-calcic alteration
Stage IIa potassic alteration
Stage IIb propylitic alteration
Stage III phyllic alteration
Stage V argillic alteration
Dimond drill hole
b
Quaternary sediments
Lower Carboniferous Jiangbasitao Fm.
Middle Devonian Beitashan Fm.
Porphyritic syenite
Quartz diorite
Diorite porphyry
Quartz granite porphyry
Shear zone
Mineralized zone
Fault
Argillic alteration zone
0
Exploration line and No.
0
4
8
12
16
20
24
N
200 m
c
N
Argillic alteration zone
Lower Carboniferous Jiangbasitao Fm.
Diorite porphyry
Argillic alteration zone
d
Quaternary sediments
Phyllic alteration zone
Argillic alteration zone
Fault

Fig. 5

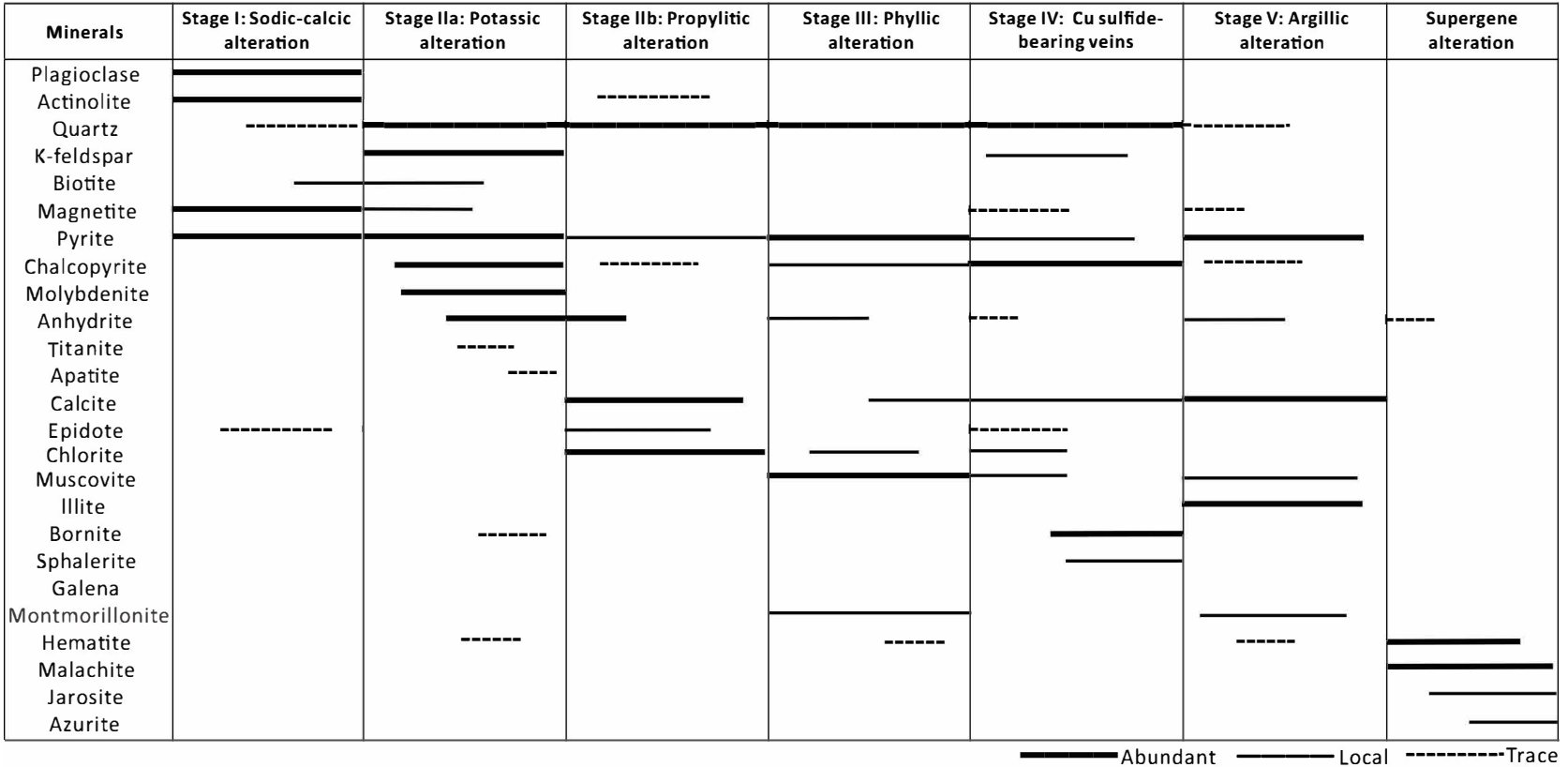
Minerals
Stage I: Sodic-calcic alteration
Stage IIa: Potassic alteration
Stage IIb: Propylitic alteration
Stage III: Phyllic alteration
Stage IV: Cu sulfide-bearing veins
Stage V: Argillic alteration
Supergene alteration
Plagioclase
Actinolite
Quartz
K-feldspar
Biotite
Magnetite
Pyrite
Chalcopyrite
Molybdenite
Anhydrite
Titanite
Apatite
Calcite
Epidote
Chlorite
Muscovite
Illite
Bornite
Sphalerite
Galena
Montmorillonite
Hematite
Malachite
Jarosite
Azurite
Abundant
Local
Trace

Fig. 4

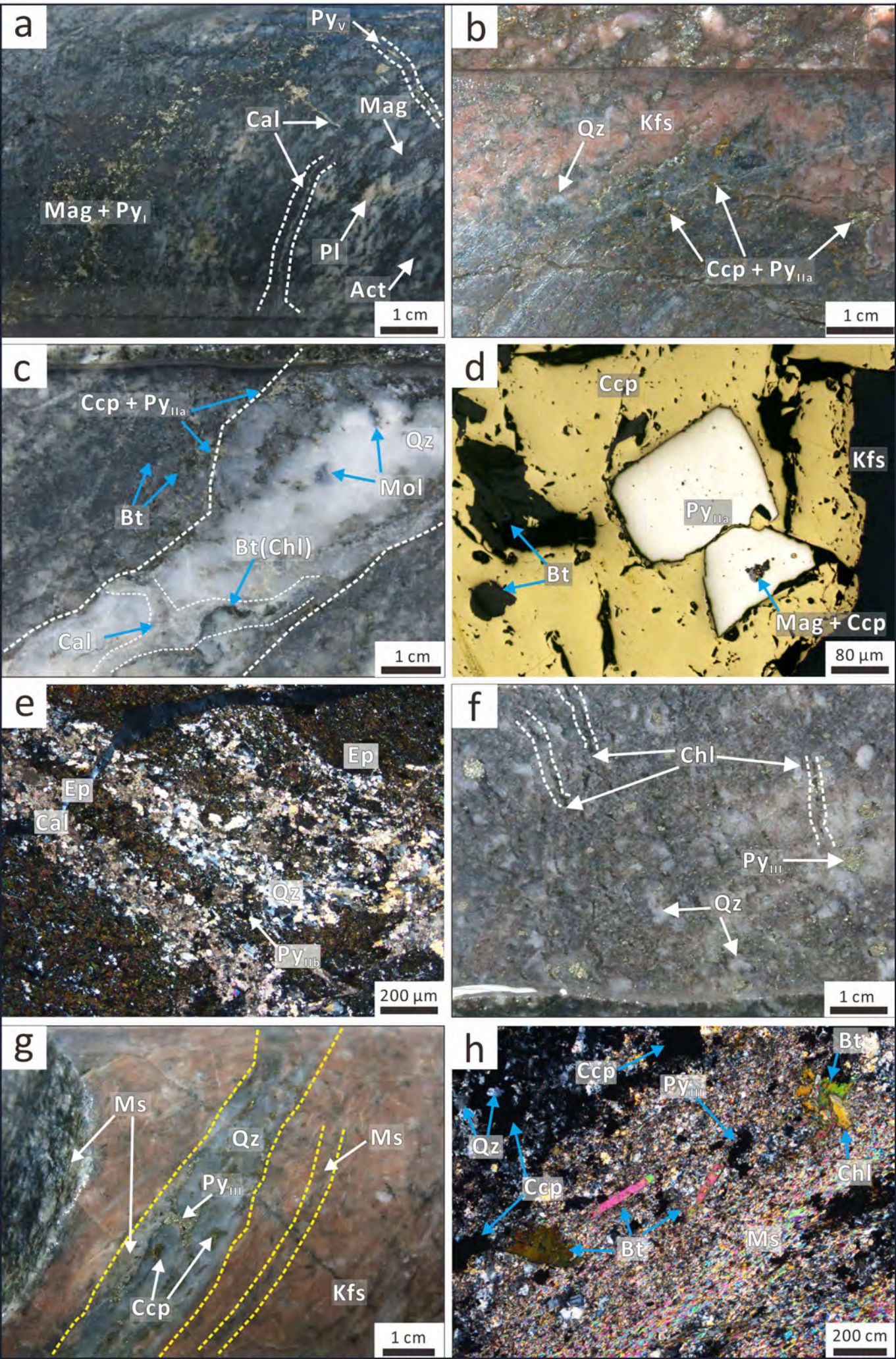
a
Py$_V$
Cal
Mag
Mag + Py$_I$
Pl
Act
1 cm
b
Qz
Kfs
Ccp + Py$_{IIa}$
1 cm
c
Ccp + Py$_{IIa}$
Qz
Mol
Bt
Bt(Chl)
Cal
1 cm
d
Ccp
Kfs
Py$_{IIa}$
Bt
Mag + Ccp
80 µm
e
Ep
Ep
Cal
Qz
Py$_{IIb}$
200 µm
f
Chl
Py$_{III}$
Qz
1 cm
g
Ms
Qz
Ms
Py$_{III}$
Ccp
Kfs
1 cm
h
Bt
Ccp
Py$_{III}$
Qz
Chl
Ccp
Bt
Ms
200 cm

Fig. 5

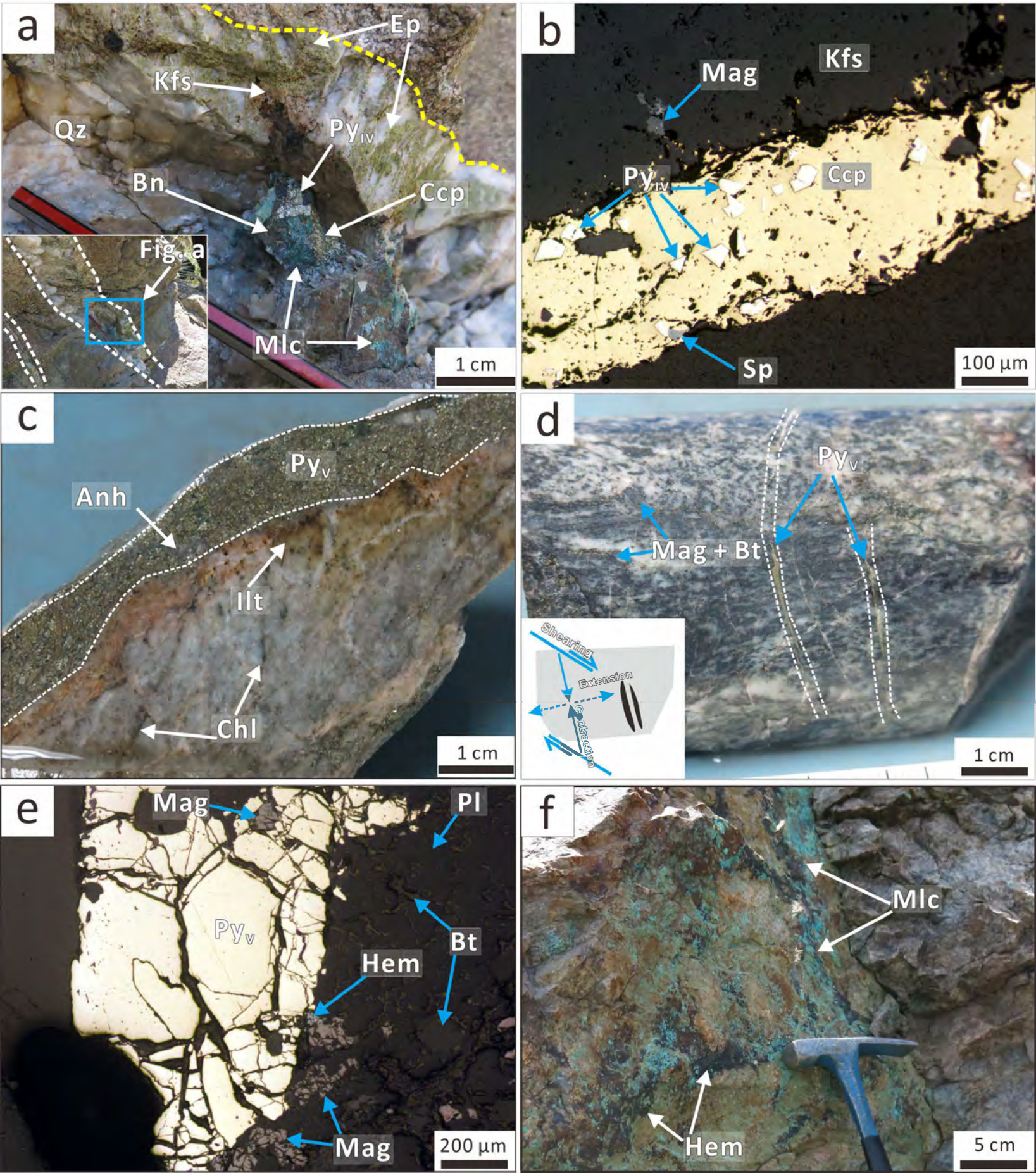
a
Ep
Kfs
Qz
Py IV
Bn
Ccp
Fig. a
Mlc
1 cm
b
Mag
Kfs
Py IV
Ccp
Sp
100 µm
c
Py V
Anh
Ilt
Chl
1 cm
d
Py V
Mag + Bt
Shearing
Extension
Contraction
1 cm
e
Mag
Pl
Py V
Bt
Hem
Mag
200 µm
f
Mlc
Hem
5 cm

Fig. 6

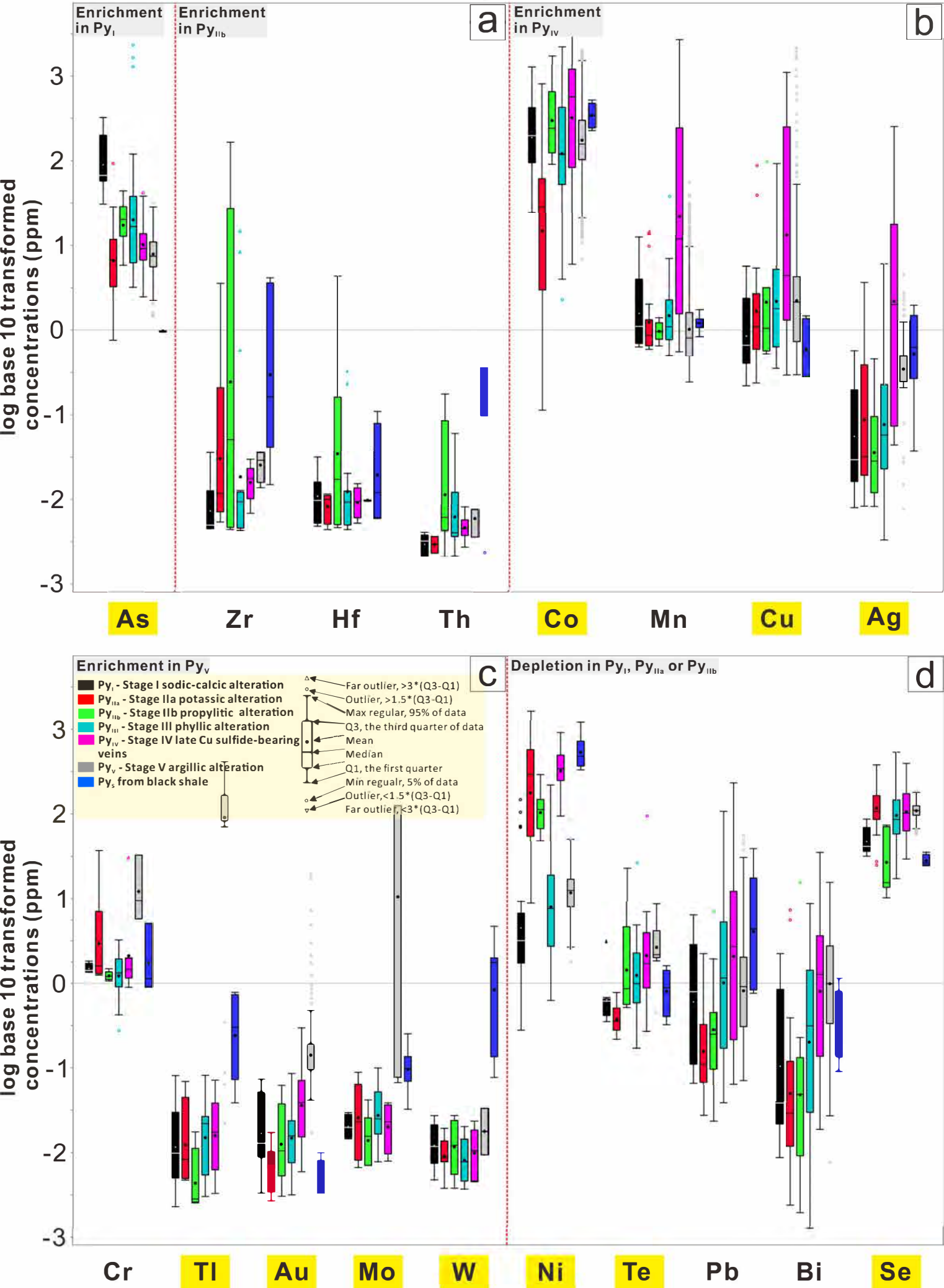
Enrichment in Py$_{I}$
Enrichment in Py$_{IIb}$
a
Enrichment in Py$_{IV}$
b
log base 10 transformed concentrations (ppm)
3
2
1
0
-1
-2
-3
As
Zr
Hf
Th
Co
Mn
Cu
Ag
Enrichment in Py$_{V}$
Py$_{I}$ - Stage I sodic-calcic alteration
Py$_{IIa}$ - Stage IIa potassic alteration
Py$_{IIb}$ - Stage IIb propylitic alteration
Py$_{III}$ - Stage III phyllic alteration
Py$_{IV}$ - Stage IV late Cu sulfide-bearing veins
Py$_{V}$ - Stage V argillic alteration
Py$_{S}$ from black shale
Far outlier, >3*(Q3-Q1)
Outlier, >1.5*(Q3-Q1)
Max regular, 95% of data
Q3, the third quarter of data
Mean
Median
Q1, the first quarter
Min regualr, 5% of data
Outlier,<1.5*(Q3-Q1)
Far outlier, <3*(Q3-Q1)
c
Depletion in Py$_{I}$, Py$_{IIa}$ or Py$_{IIb}$
d
Cr
Tl
Au
Mo
W
Ni
Te
Pb
Bi
Se

Fig. 7

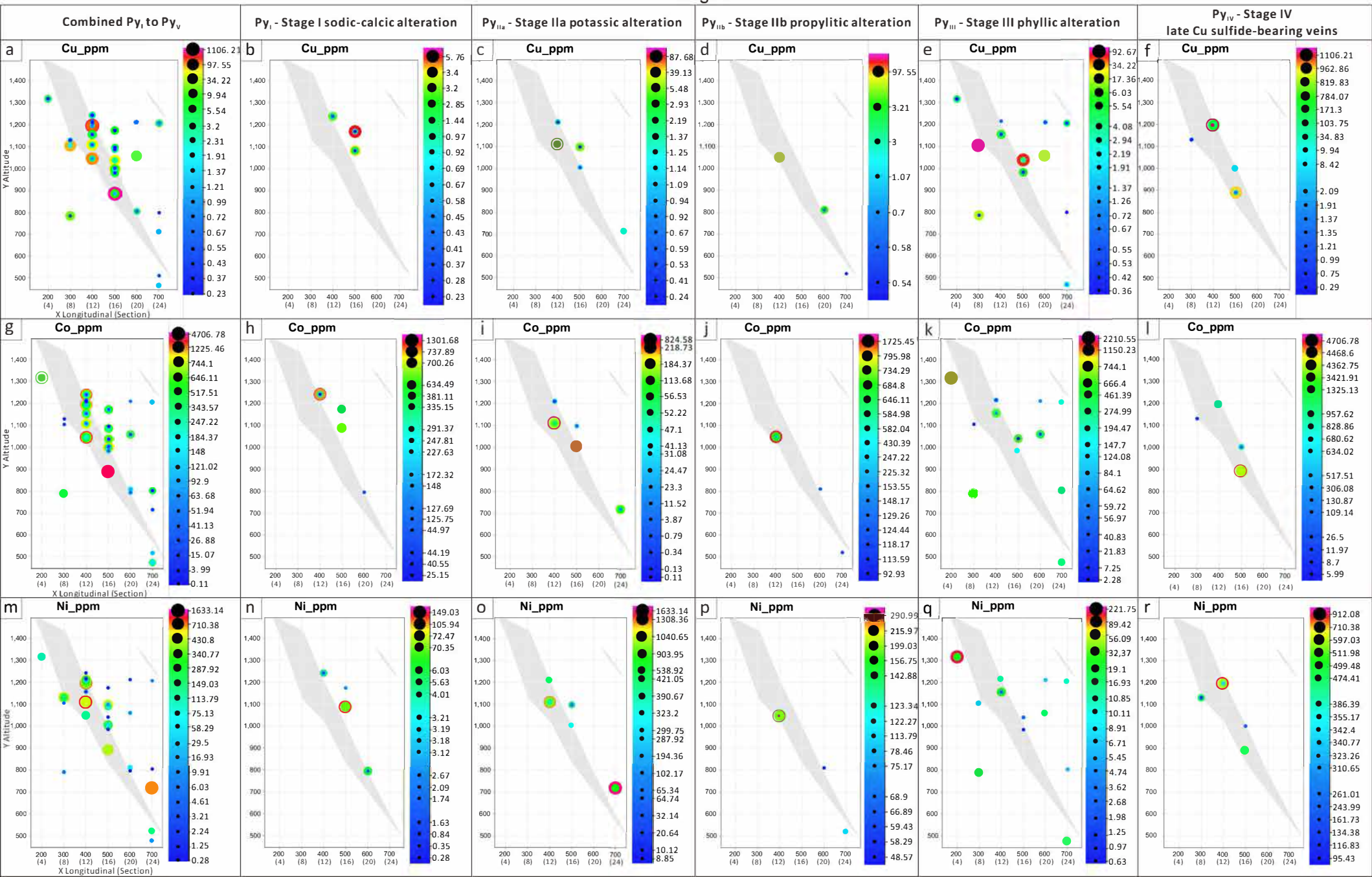
Combined Py$_I$ to Py$_V$
Py$_I$ - Stage I sodic-calcic alteration
Py$_{IIa}$ - Stage IIa potassic alteration
Py$_{IIb}$ - Stage IIb propylitic alteration
Py$_{III}$ - Stage III phyllic alteration
Py$_{IV}$ - Stage IV late Cu sulfide-bearing veins
a Cu_ppm
b Cu_ppm
c Cu_ppm
d Cu_ppm
e Cu_ppm
f Cu_ppm
g Co_ppm
h Co_ppm
i Co_ppm
j Co_ppm
k Co_ppm
l Co_ppm
m Ni_ppm
n Ni_ppm
o Ni_ppm
p Ni_ppm
q Ni_ppm
r Ni_ppm
Y Altitude
X Longitudinal (Section)

Fig. 8

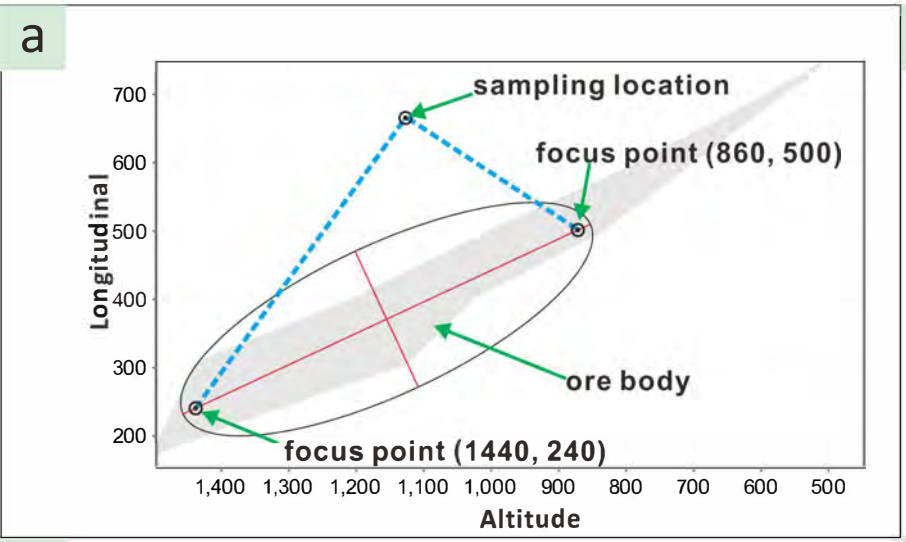
a
sampling location
focus point (860, 500)
ore body
focus point (1440, 240)
Longitudinal
Altitude
700
600
500
400
300
200
1,400
1,300
1,200
1,100
1,000
900
800
700
600
500

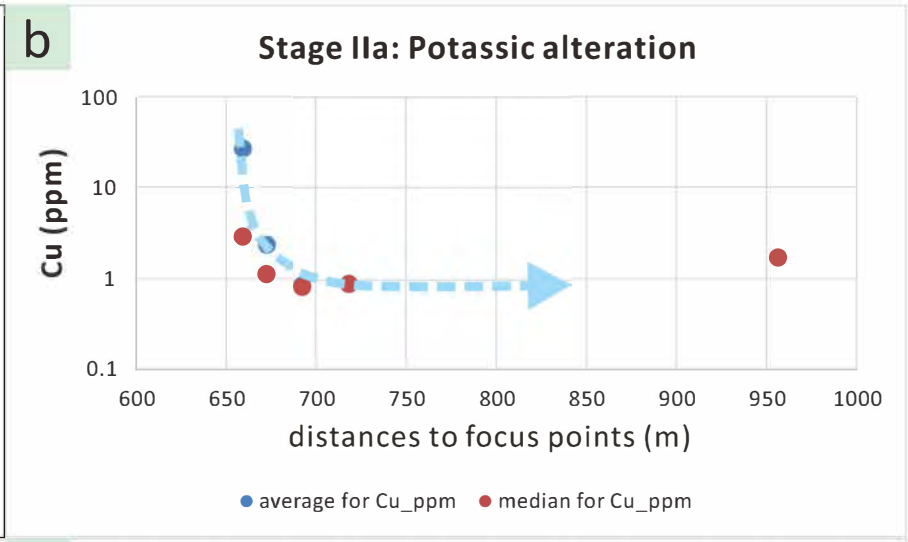
b
Stage IIa: Potassic alteration
Cu (ppm)
100
10
1
0.1
600
650
700
750
800
850
900
950
1000
distances to focus points (m)
average for Cu_ppm
median for Cu_ppm

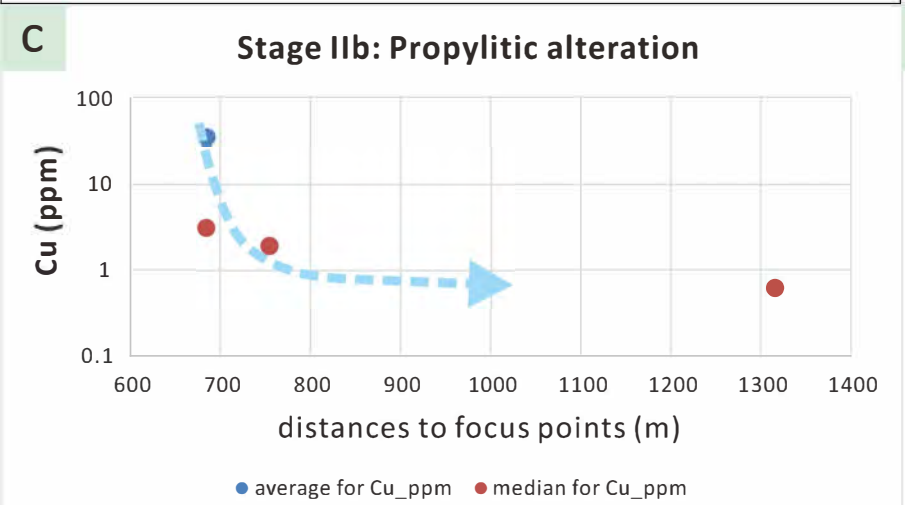
c
Stage IIb: Propylitic alteration
Cu (ppm)
100
10
1
0.1
600
700
800
900
1000
1100
1200
1300
1400
distances to focus points (m)
average for Cu_ppm
median for Cu_ppm

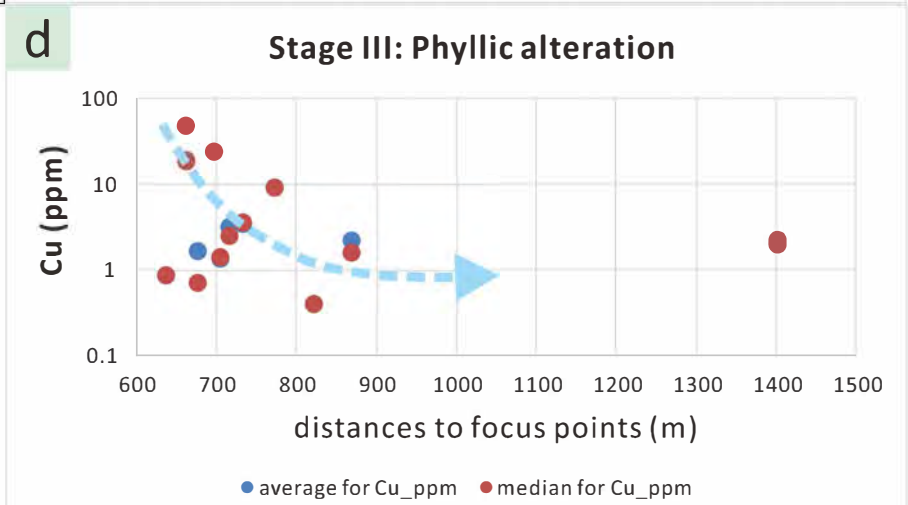
d
Stage III: Phyllic alteration
Cu (ppm)
100
10
1
0.1
600
700
800
900
1000
1100
1200
1300
1400
1500
distances to focus points (m)
average for Cu_ppm
median for Cu_ppm

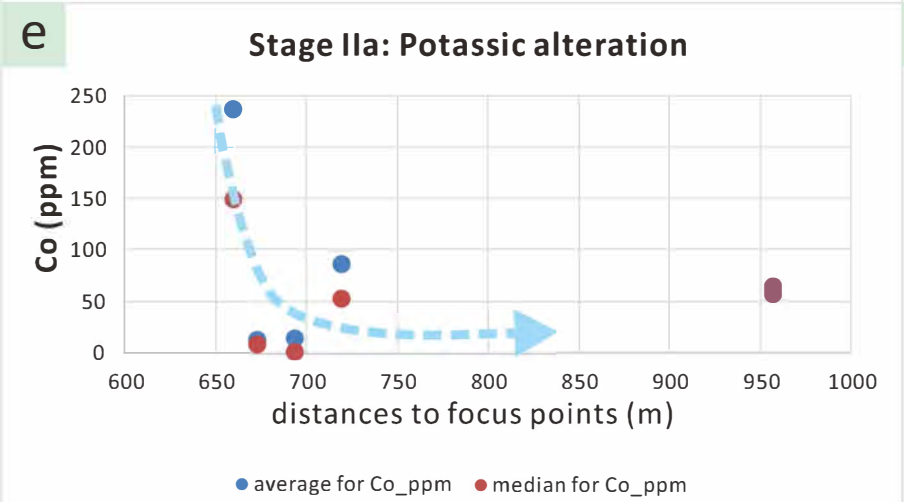
e
Stage IIa: Potassic alteration
Co (ppm)
250
200
150
100
50
0
600
650
700
750
800
850
900
950
1000
distances to focus points (m)
average for Co_ppm
median for Co_ppm

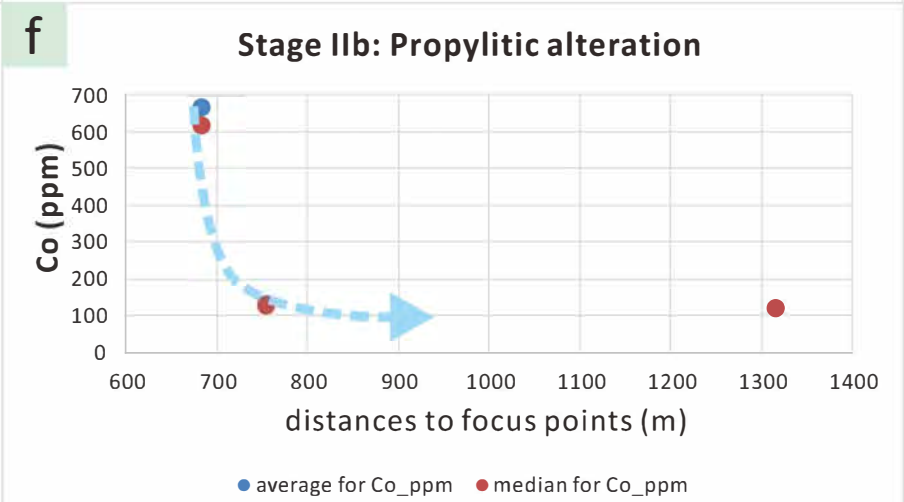
f
Stage IIb: Propylitic alteration
Co (ppm)
700
600
500
400
300
200
100
0
600
700
800
900
1000
1100
1200
1300
1400
distances to focus points (m)
average for Co_ppm
median for Co_ppm

Fig. 9

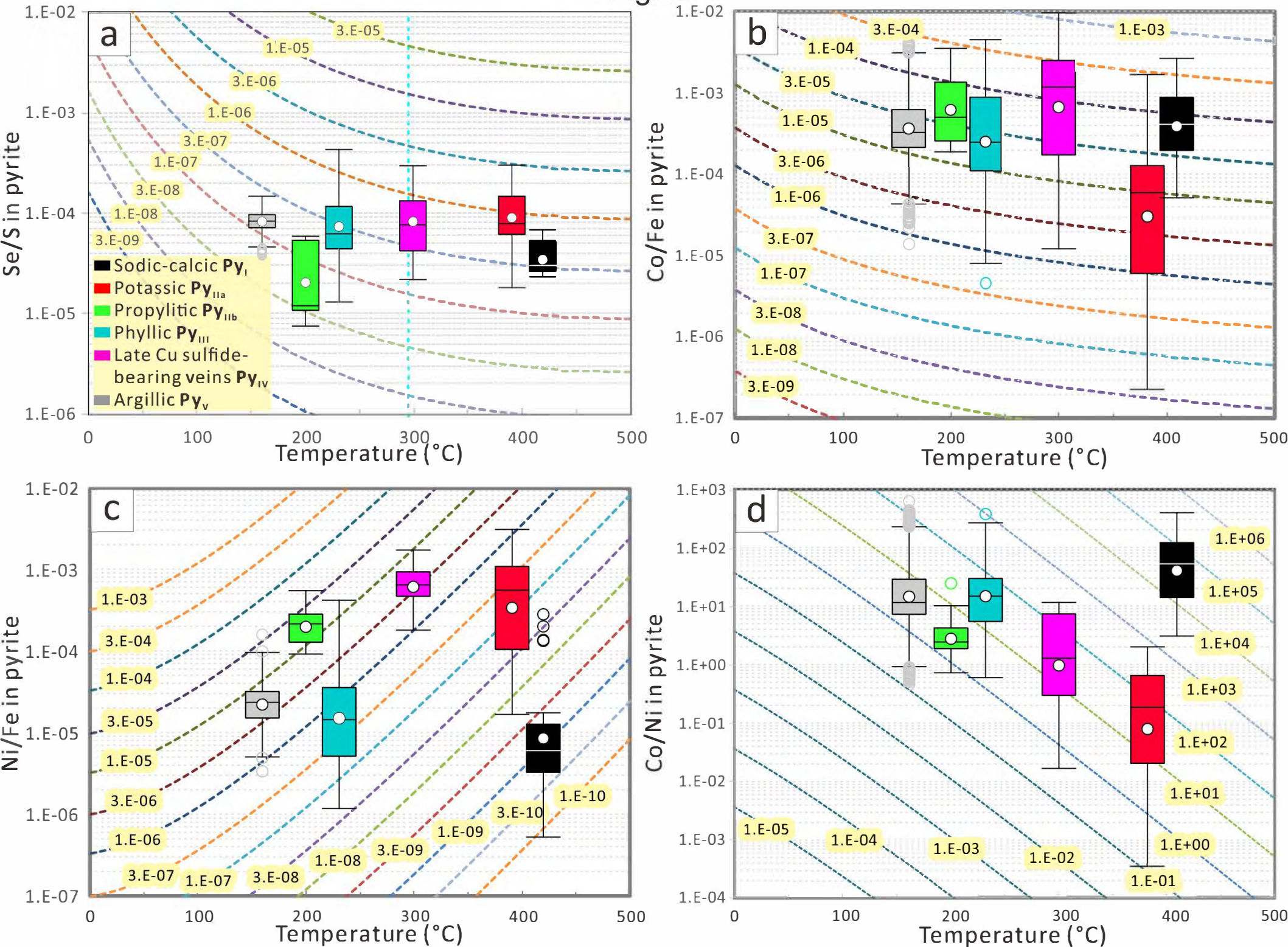
a
Se/S in pyrite
Temperature (°C)
Sodic-calcic Py$_{I}$
Potassic Py$_{IIa}$
Propylitic Py$_{IIb}$
Phyllic Py$_{III}$
Late Cu sulfide-bearing veins Py$_{IV}$
Argillic Py$_{V}$
b
Co/Fe in pyrite
Temperature (°C)
c
Ni/Fe in pyrite
Temperature (°C)
d
Co/Ni in pyrite
Temperature (°C)

Fig. 10

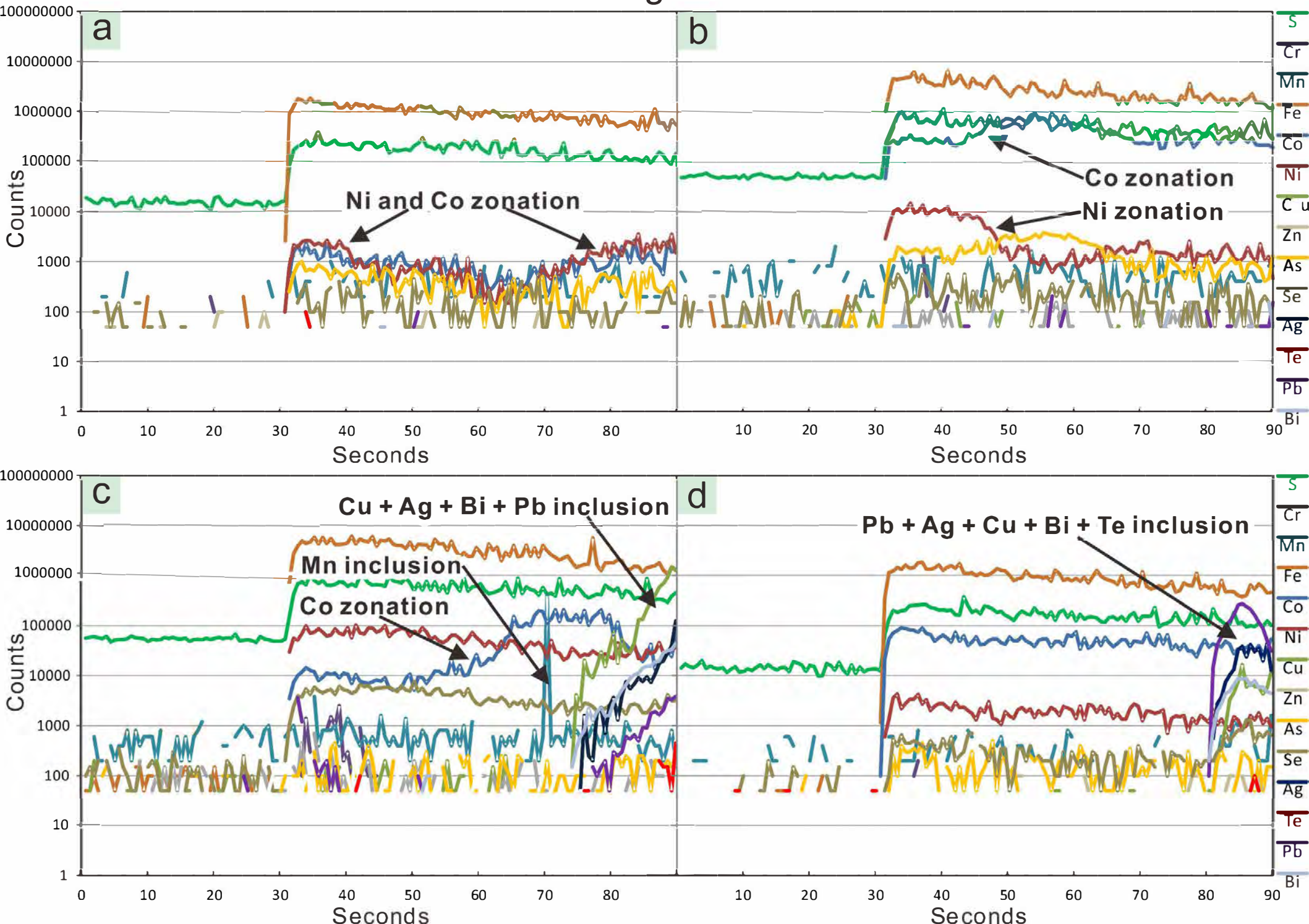
a
b
c
d
Counts
Seconds
Ni and Co zonation
Co zonation
Ni zonation
Cu + Ag + Bi + Pb inclusion
Mn inclusion
Co zonation
Pb + Ag + Cu + Bi + Te inclusion
S
Cr
Mn
Fe
Co
Ni
Cu
Zn
As
Se
Ag
Te
Pb
Bi

Fig. 11

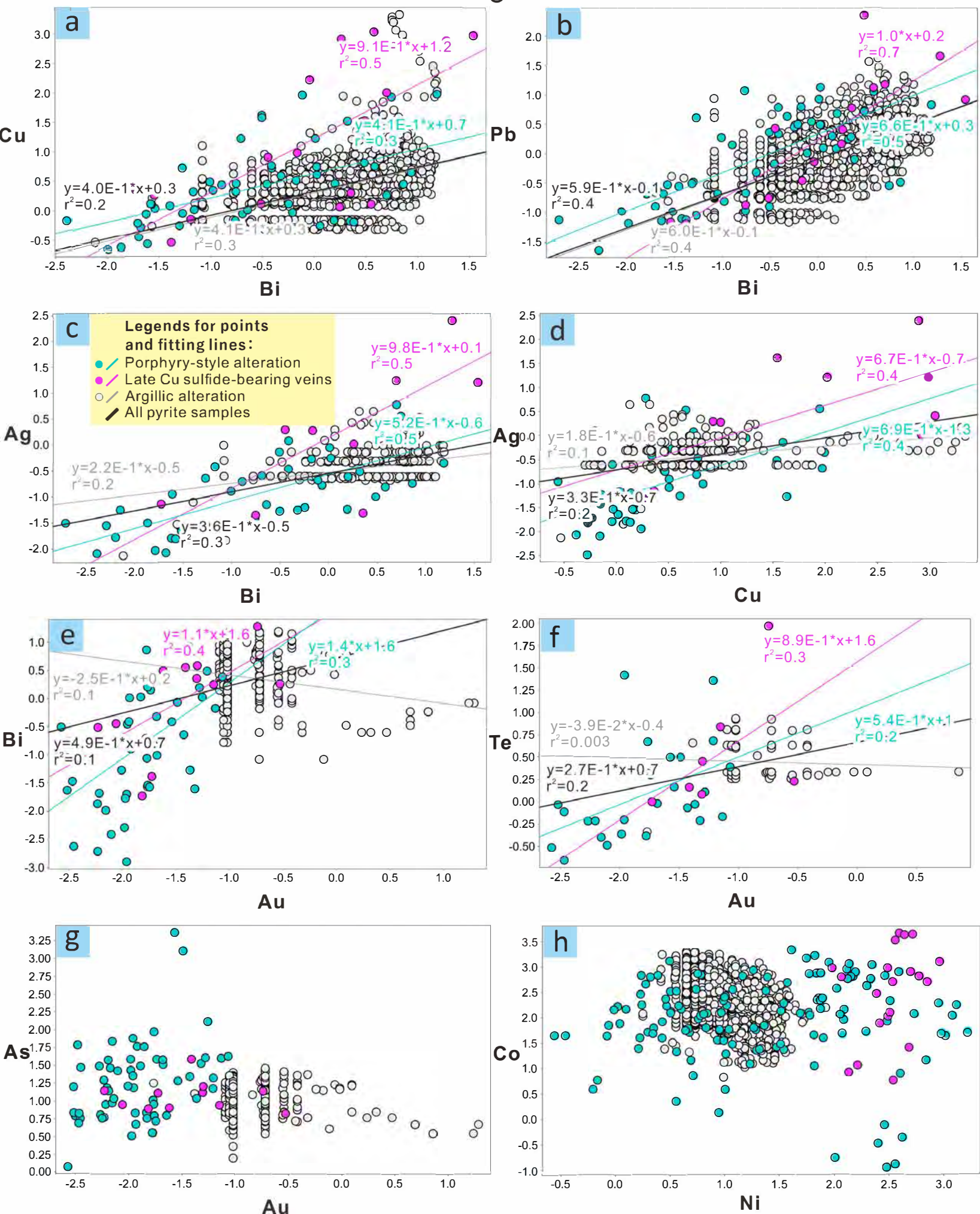
a
y=9.1E-1*x+1.2
r²=0.5
y=4.1E-1*x+0.7
r²=0.3
y=4.0E-1*x+0.3
r²=0.2
y=4.1E-1*x+0.3
r²=0.3
Cu
Bi
b
y=1.0*x+0.2
r²=0.7
y=6.6E-1*x+0.3
r²=0.5
y=5.9E-1*x-0.1
r²=0.4
y=6.0E-1*x-0.1
r²=0.4
Pb
Bi
c
Legends for points and fitting lines:
Porphyry-style alteration
Late Cu sulfide-bearing veins
Argillic alteration
All pyrite samples
y=9.8E-1*x+0.1
r²=0.5
y=5.2E-1*x-0.6
r²=0.5
y=2.2E-1*x-0.5
r²=0.2
y=3.6E-1*x-0.5
r²=0.3
Ag
Bi
d
y=6.7E-1*x-0.7
r²=0.4
y=6.9E-1*x-1.3
r²=0.4
y=1.8E-1*x-0.6
r²=0.1
y=3.3E-1*x-0.7
r²=0.2
Ag
Cu
e
y=1.1*x+1.6
r²=0.4
y=1.4*x+1.6
r²=0.3
y=-2.5E-1*x+0.2
r²=0.1
y=4.9E-1*x+0.7
r²=0.1
Bi
Au
f
y=8.9E-1*x+1.6
r²=0.3
y=-3.9E-2*x-0.4
r²=0.003
y=5.4E-1*x+1
r²=0.2
y=2.7E-1*x+0.7
r²=0.2
Te
Au
g
As
Au
h
Co
Ni

Fig. 12

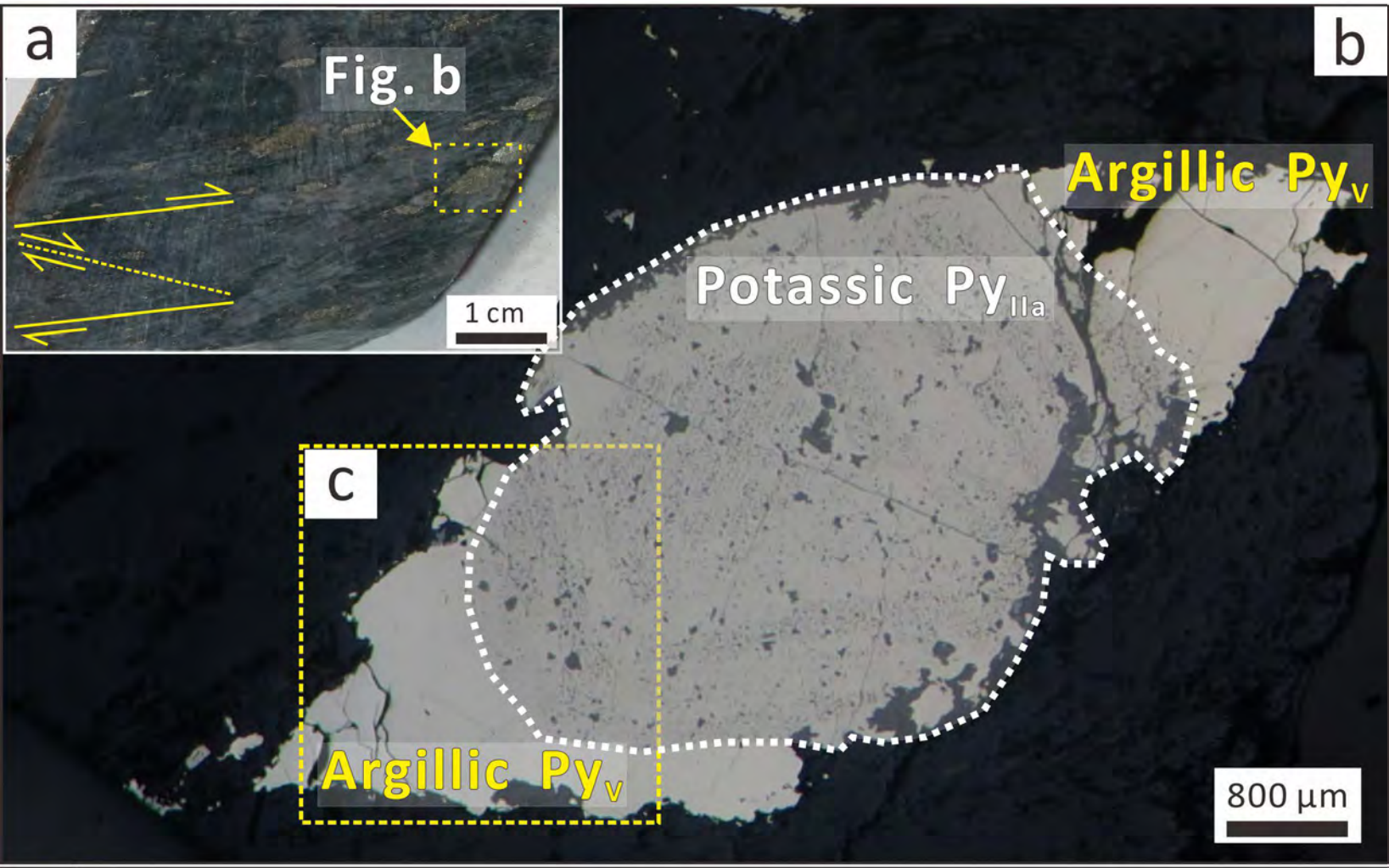
a
Fig. b
1 cm
b
Argillic Py$_V$
Potassic Py$_{IIa}$
C
Argillic Py$_V$
800 µm

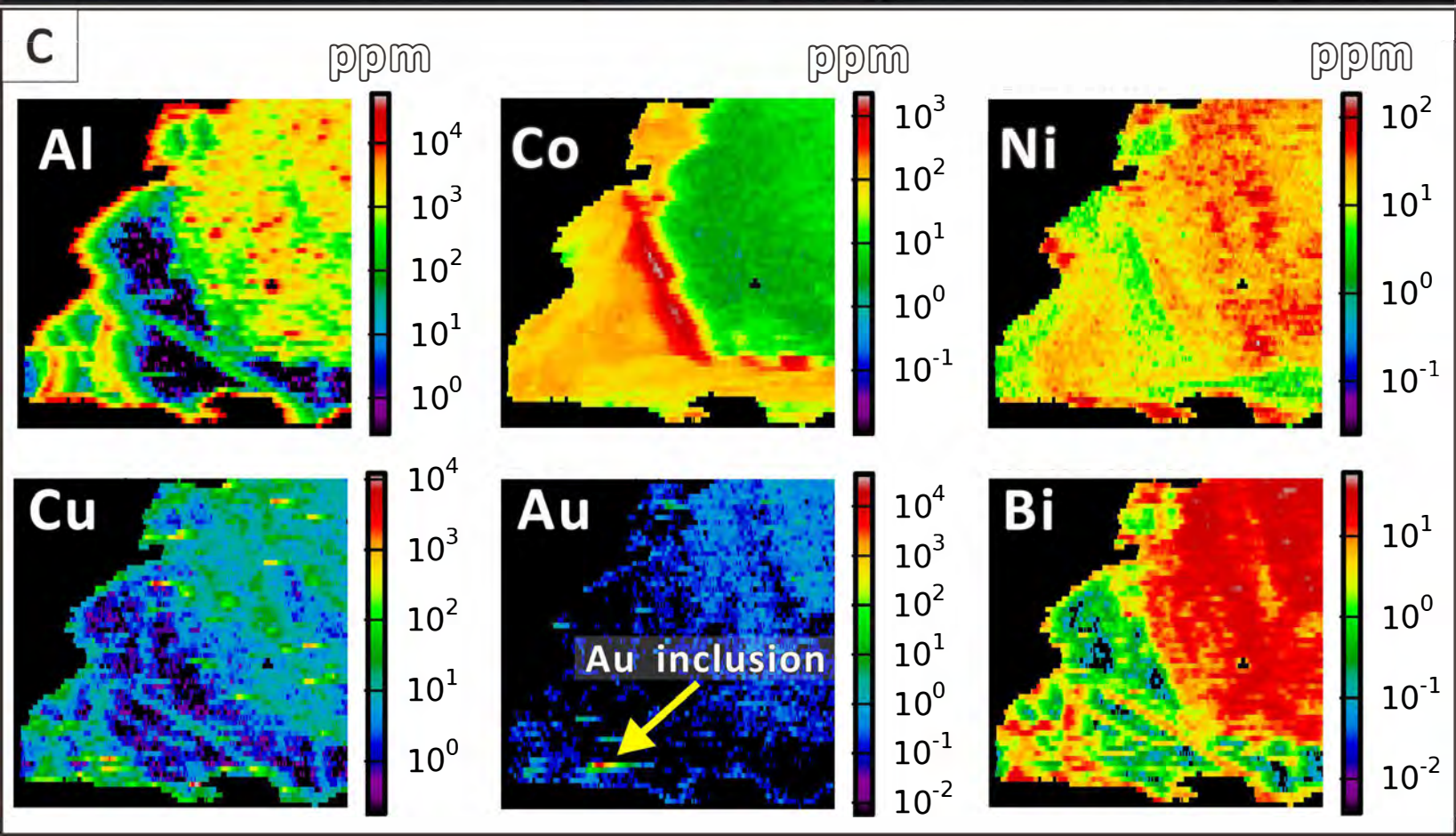
c
ppm
Al
10^4 10^3 10^2 10^1 10^0
ppm
Co
10^3 10^2 10^1 10^0 10^{-1}
ppm
Ni
10^2 10^1 10^0 10^{-1}
Cu
10^4 10^3 10^2 10^1 10^0
Au
Au inclusion
10^4 10^3 10^2 10^1 10^0 10^{-1} 10^{-2}
Bi
10^1 10^0 10^{-1} 10^{-2}

Fig. 13

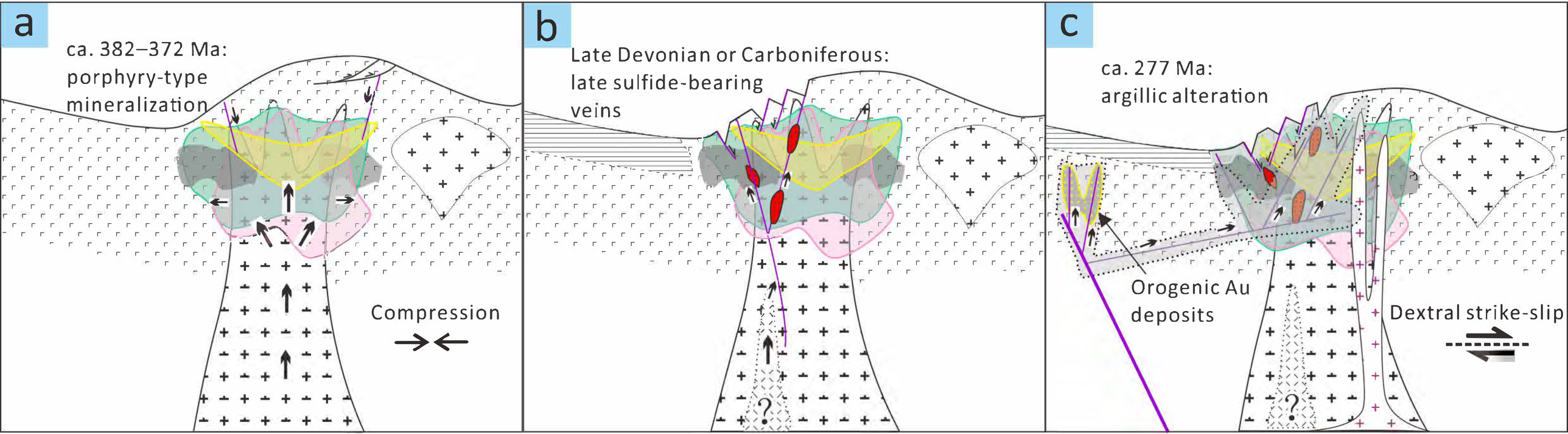

Devonian volcanic rocks

Carboniferous sediments

Pre-mineralization porphyritic syenite

Syn-mineralization intrusions

Post-mineralization alkali granite porphyry

Inferred blind intrusions

Na-Ca alteration

Potassic alteration

Propylitic alteration

Phyllic alteration

Late sulfide-bearing veins

Argillic alteration

Orogenic Au deposit

Inferred fault

Fluid migration path